

# Electrically tunable resonant scattering in fluorinated bilayer graphene

Adam A. Stabile<sup>1</sup>, Aires Ferreira<sup>2,3,\*</sup>, Jing Li<sup>1</sup>, N. M. R. Peres<sup>3</sup>, and J. Zhu<sup>1,4†</sup>

<sup>1</sup>*Department of Physics, The Pennsylvania State University, University Park, Pennsylvania 16802, USA*

<sup>2</sup>*Department of Physics, University of York, York YO10 5DD, United Kingdom*

<sup>3</sup>*Centro de Física and Departamento de Física, Universidade do Minho, Campus de Gualtar, Braga 4710-057, Portugal and*

<sup>4</sup>*Center for 2-Dimensional and Layered Materials, The Pennsylvania State University, University Park, Pennsylvania 16802, USA*

Adatom-decorated graphene offers a promising new path towards spintronics in the ultrathin limit. We combine experiment and theory to investigate the electronic properties of dilutely fluorinated bilayer graphene, where the fluorine adatoms covalently bond to the top graphene layer. We show that fluorine adatoms give rise to resonant impurity states near the charge neutrality point of the bilayer, leading to strong scattering of charge carriers and hopping conduction inside a field-induced band gap. Remarkably, the application of an electric field across the layers is shown to tune the resonant scattering amplitude from fluorine adatoms by nearly twofold. The experimental observations are well explained by a theoretical analysis combining Boltzmann transport equations and fully quantum-mechanical methods. This paradigm can be generalized to many bilayer graphene-adatom materials, and we envision that the realization of electrically tunable resonance may be a key advantage in graphene-based spintronic devices.

PACS numbers: 72.80.Vp, 72.10.Fk

Chemical functionalization is a powerful tool to engineer graphene for a broad range of application needs. The attachment of oxygen groups makes graphene soluble and fluorescent, and facilitates the formation of graphene nanocomposites [1–3]. Chemisorbed species increase the degree of  $sp^3$  bonding, drastically affecting graphene's electrical conductivity, mechanical strength, and optical response, even in the very dilute limit [4–22]. The deposition of light adatoms, such as hydrogen and fluorine, endows graphene with intriguing magnetic and spintronic properties, including localized magnetic moments and enhanced spin-orbit coupling, which may enable the generation of large spin currents [16–19, 21–24].

Covalently bonded monovalent species, with orbitals close to the Dirac point of graphene systems, effectively decouple their carbon host from its neighbors, thereby simulating vacancies [25]. The latter are predicted to introduce power-law localized midgap states at the Dirac point [26–28], displaying anomalous divergent behavior of the density of states [29, 30]. These so-called resonant scatterers have a profound impact on charge carrier transport at all carrier densities, invalidating conventional transport pictures based on the weak disorder hypothesis [31–33]. In the high carrier density regime  $|n| \gg n_{rs}$ , where  $n_{rs}$  denotes the areal density of resonant scatterers, the dc conductivity deviates from its typical behaviour  $\sigma \propto |n|$ , acquiring a robust sublinear dependence, owing to a nonperturbative renormalization of  $s$ -wave phase shifts:  $\delta_0(n) \approx \pi/[2 \ln(R\sqrt{\pi|n|})]$ , where  $R \approx 0.4$  nm is the scatterer range [18, 25, 31, 32].

Resonant scattering also plays an important role in metal spintronics [34], although such interactions are not easily tunable. Engineering tunable resonant interaction of charge carriers with atomic impurities in graphene *in*

*situ* would open new avenues, including the harnessing of spin relaxation [35] and the generation of robust spin currents through the extrinsic spin Hall effect [23, 24]. From the viewpoint of device scaling and operations, it is particularly desirable to implement gate-controlled resonant interactions. A suitable candidate—so far overlooked—is bilayer graphene (BLG). Adatoms in BLG are likewise predicted to induce resonant scattering [32, 36, 37]. Moreover, the presence of two layers allows the mirror symmetry to be broken by an electric field perpendicular to the layers, opening up a band gap up to 250 meV [38–42]. The consequences of this extra degree of freedom for resonant scattering remain largely unexplored.

In this Rapid Communication, we report experimental observations of adatom-limited charge transport in BLG using fluorine adatoms as an example. Dual gating allows us to control the carrier type, density, and the perpendicular (bias) electric field independently. Both experiment and theory demonstrate that fluorine adatoms behave as resonant scatterers. Moreover, we show that the charge carrier scattering amplitude becomes strongly electron-hole asymmetric and is tunable over a large range  $\pm 20 - 30\%$  by controlling the carrier distribution between the two layers using a bias electric field. Once more, theory and experiment are found to be in excellent agreement. The demonstrated electric tunability of the resonant cross section offers a convenient tool to engineer desired charge-spin responses in graphene-adatom systems.

Bilayer graphene flakes are exfoliated from bulk highly ordered pyrolytic graphite (HOPG graphite) (ZYA grade, SPI supplies) onto prefabricated HfO<sub>2</sub>/Au bottom gate stacks [43], optically identified and confirmed by Raman spectroscopy. The flakes are then fluorinated in a CF<sub>4</sub>

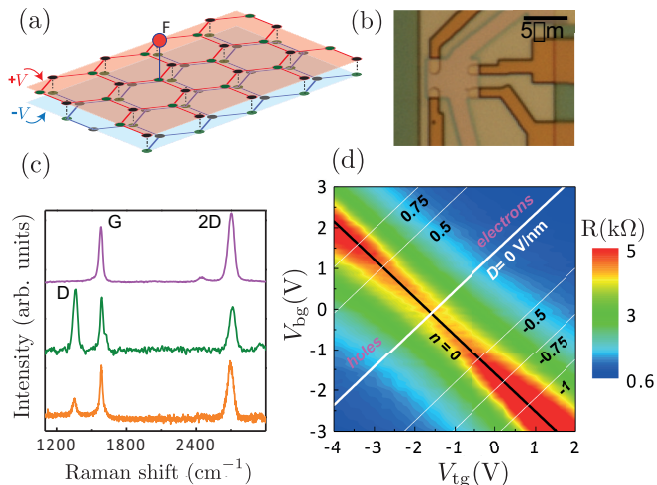


Figure 1: Single-sided fluorinated BLG. (a) Schematic. Solid (dashed) lines represent the intralayer (interlayer) hopping terms. Fluorine adatoms bond to carbon hosts at random positions. (b) Optical micrograph of sample W02 showing the Au bottom gate (wide yellow stripe), four Au electrodes to the sample (dark gold) in van der Pauw geometry, and the top gate connected to two Au electrodes (yellow). (c) Raman spectra of pristine (plum), fluorinated (olive, from sample W02) and defluorinated (orange) BLG. The laser excitation wavelength is 488 nm.  $I_D/I_G=1.15$  for W02 and 0.3 for the defluorinated sample. (d) The color map of a four-terminal resistance  $R$  as a function of the top and bottom gate voltages. The black line corresponds to  $n=0$  and the white lines correspond to constant bias  $D$  fields.  $T=10$  K. From W38.

plasma asher where fluorine atoms covalently bond with carbon atoms in the top layer only [see Fig. 1(a)]. Bilayer graphene is substantially harder to fluorinate compared to monolayer graphene [17]. Discussions of the plasma conditions are given in the Supplemental Material (SM) [44]. After fluorination, ver der Pauw or Hall bar devices are completed using standard  $e$ -beam lithography and atomic layer deposition techniques [42, 43]. Results from three fluorinated samples (W02, W03, and W38) and one defluorinated sample Df are reported here. An optical micrograph of device W38 is shown in Fig. 1(b). Fig. 1(c) plots the Raman spectra of a pristine bilayer, device W02, and a typical trace from a defluorinated bilayer; see Supplemental Material and Ref. [17] for defluorination recipe. Following the atomic defect density calibration obtained by Lucchese *et al.* on monolayers [45] and taking into account the doubling of the G band intensity in bilayer, we estimate a fluorine areal density  $n_F^{\text{ram}} \approx 3.3 \times 10^{12} \text{ cm}^{-2}$  for device W02, and the unintentional defect density (e.g., vacancy), as seen in the defluorinated bilayer, is roughly  $0.6 \times 10^{12} \text{ cm}^{-2}$ . Parameters from all four samples are given in Table I of the Supplemental Material. We use standard low-frequency, low excitation lock-in techniques to carry out electrical transport measurements at temperatures ranging from

1.6 K to 200 K. A false color map of a four-terminal resistance  $R$  in sample W38 as a function of the top and bottom gate voltages  $V_{\text{tg}}$  and  $V_{\text{bg}}$  is shown in Fig. 1 (d) and displays characteristics similar to that of a pristine bilayer [42]. This map enables us to extract the dependence of the sheet conductance  $\sigma_s$  on the carrier density  $n$  at fixed bias  $D$  fields.

*Resonant impurity scattering.*—We first establish the resonant impurity nature of the fluorine adatoms. The rearrangement of electronic spectral weight due to the fluorination can be estimated through a calculation of the density of states (DOS) for a typical adatom concentration. To model the BLG system we employ a nearest-neighbor tight-binding Hamiltonian of  $\pi$  electrons, supplemented with an on-site energy term  $\pm V$  in the top (bottom) layer describing the effect of the  $D$  field. Fluorine adatoms are modeled as vacancies in the top layer [25, 32]. The kernel polynomial method [46] is then used to accurately extract the DOS of a large lattice with  $2 \times 14142^2$  carbon atoms. Details of the calculation are given in the Supplemental Material.

The calculated DOS is shown in Fig. 2(a). We note two prominent features. Firstly, in unbiased BLG, the DOS displays a sharp peak centered at zero energy (midgap state), already encountered in Refs. [32, 47]. Secondly, at nonzero bias field, new resonances pile up at the edges of the pseudogap, which is consistent with results obtained for a single vacancy [28]. Due to the broken layer symmetry, these resonances have different weights at  $E_F \approx \pm V$ , anticipating substantial electron-hole asymmetry (EHA). Fig. 2(b) shows  $\sigma_s(n)$  at  $D = 0$  for samples W38, W02, W03, and Df at  $T = 1.6$  K. Sample Df has a field effect mobility of  $\mu \approx 1600 \text{ cm}^2/\text{Vs}$ , which is comparable to that of a pristine bilayer in a similar geometry [42]. In contrast, fluorinated bilayers display much lower mobility: 172, 100, and 86  $\text{cm}^2/\text{Vs}$  for W38, W02, and W03, respectively, which signals the dominance of adatom-induced scattering. Ferreira *et al.* [32] showed that in the high carrier density regime  $n > n_F$  where quantum corrections are not dominant, a semiclassical description applies, and the resonant-scattering-limited sheet conductivity in unbiased BLG is given by

$$\sigma_s(n) = 2 \times \frac{\pi e^2 |n|}{4h n_F}, \quad (1)$$

where an extra factor of 2 accounts for the one-sided fluorination of our samples. Since  $\sigma_s$  is approximately insensitive to the scatterer radius, there is a single fitting parameter,  $n_F$ . Fits to Eq. 1 are plotted as dashed lines in Fig. 2(b) and describe data very well at high density [32]. The extracted  $n_F$  are in good agreement with values obtained from Raman spectra for all samples (see Table I in Supplemental Material). Furthermore, in all samples we find an  $n_F$ -independent  $\sigma_s \approx e^2/h$  in the low carrier density regime  $n < n_F$ , also in agreement with

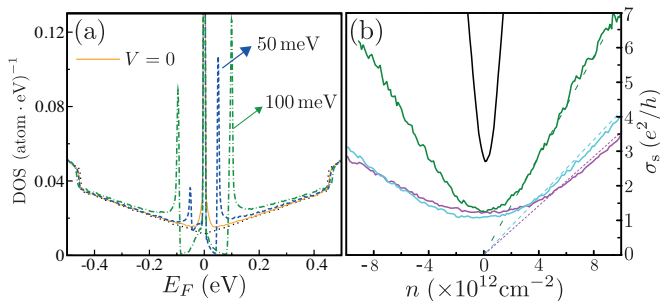


Figure 2: Resonant impurity scattering in fluorinated BLG. (a) Calculated DOS of macroscopic size ( $\approx \mu\text{m}^2$ ) BLG system as a function of the Fermi energy at selected bias potential values for a F:C ratio of 1:2000. The DOS of pristine unbiased BLG is also shown (black dotted line). (b)  $\sigma_s(n)$  in samples (from top to bottom): Df (black), W38 (olive), W02 (cyan) and W03 (plum) at  $T = 1.6$  K. Positive  $n$  corresponds to electron doping. Dashed lines of the same color are fits to Eq. (1).

theory. This observation is consistent with the formation of a narrow “impurity band” around the charge neutrality point (CNP) [32, 47] [see thick (orange) line in Fig. 2(a)].

More direct evidence of the impurity band is seen in the temperature-dependent resistance of the CNP under a finite bias field. Figure 3(a) plots  $R_{\text{CNP}}(D)$ —the sheet resistance of the CNP in sample W02—as a function of  $D$  at selected temperatures  $T = 1.6$ –200 K, together with  $R_{\text{CNP}}(D)$  of sample Df at  $T = 1.6$  K.  $R_{\text{CNP}}(D)$  of sample Df is similar to that of a pristine bilayer [42].  $R_{\text{CNP}}(D)$  of W02, on the other hand, rises much more slowly, pointing to additional conduction channels inside the band gap. To further understand the behavior of  $R_{\text{CNP}}$ , we plot in Fig. 3(b) its temperature dependence in both samples at  $D = 0.93$  V/nm. The most remarkable difference between the two lies at high temperatures  $T > 50$  K. In this regime, sample Df exhibits activated transport  $R_1 \propto \exp(E_1/k_B T)$ , with  $E_1$  increasing with  $D$  from 22.5 meV at  $D = 0$  (data not shown) to 33.5 meV at  $D = 0.93$  V/nm. These values are similar to pristine bilayers, where  $\Delta = 2E_1$  approximates the bias-induced band gap in the large  $D$  limit [42]. In contrast, similar analyses done on  $R_{\text{CNP}}(T)$  of the three fluorinated bilayers yield roughly  $D$ -independent  $E_1$ , which is approximately 11–13 meV in all samples. We attribute this behavior to nearest-neighbor hopping among the fluorine-induced impurity states, as illustrated in the inset to Fig. 3(b), where  $E_1$  is the half-width of the impurity band. This mechanism effectively shunts the band edge activation  $\exp(\Delta/2k_B T)$  to result in a  $D$ -independent  $R_{\text{CNP}}(T)$ . Counting two impurity states per adatom [32], we independently estimate the bandwidth to be  $\approx 10$  meV at  $n_F \approx 4 \times 10^{12} \text{ cm}^{-2}$ , which is in excellent agreement with the  $E_1$  values extracted here.

*Electric-field tuning of resonant scattering.*—Next, we explore the role of a bias  $D$  field in the carrier density

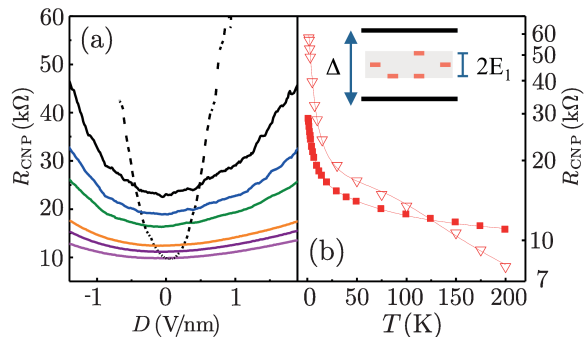


Figure 3: Charge carrier transport at the CNP. (a)  $R_s$  vs  $D$  at the CNP for sample Df (dashed line,  $T=1.6$  K) and sample W02 (solid lines). From top to bottom:  $T=1.6$  K (black), 5 K (blue), 10 K (olive), 50 K (orange), 100 K (purple) and 200 K (plum). (b)  $R_s(T)$  of sample Df (open triangles) and sample W02 (solid squares) at  $D=0.93$  V/nm. The solid lines are fits to Eq.(1) of Ref. [42].  $E_1=11$  meV and 33.5 meV for samples W02 and Df, respectively. Inset: A schematic diagram of the fluorine-induced impurity states inside the field-induced band gap of a bilayer graphene.

regime  $n > n_F$ . Figure 4(a) plots  $\sigma_s(n)$  of sample W02 at selected  $D$ 's from  $-2$  to  $2$  V/nm, where  $D > 0$  indicates field pointing towards the fluorine adatoms, as the inset of (a) shows. Pronounced EHA is observed. For electrons,  $\sigma_s$  increases (decreases) when  $D > 0$  ( $D < 0$ ) and the opposite trend is observed for holes. This  $D$ -field tuning is further illustrated in Fig. 4(b), where we plot the normalized conductance change  $\delta\sigma_s(D) \equiv \Delta\sigma_s(D)/\sigma_s(0) = [\sigma_s(D) - \sigma_s(0)]/\sigma_s(0)$  of the data in Figure 4 (a). Strikingly, in the high-density regime,  $\delta\sigma_s(D)$  is roughly  $n$ -independent and ranges between  $-0.35$  and  $0.2$  for  $|D| < 2$  V/nm, i.e., the change of  $\sigma_s$  is nearly twofold. Furthermore,  $\delta\sigma_s(D)$  appears to be symmetric under  $(n, D) \rightarrow (-n, -D)$ . Similar  $D$ -field tuning of  $\sigma_s(n)$  is observed on all three fluorinated samples, with the magnitude of  $\delta\sigma_s(D)$  varying within a factor of 2 among them. Further examination of the EHA rules out an extrinsic mechanism due to nonuniform density distribution created by electrodes that screen a portion of the top gate. The detailed discussions are given in the Supplemental Material. Intuitively, the experimental observations suggest an increased weight of hole (electron) wave functions in the top layer under a positive (negative)  $D$  field, and thus increased resonant impurity scattering.

To gain further insight into the strong  $D$ -field tuning of charge carrier transport, we solve analytically the Boltzmann transport equations for a BLG system with random short-range impurities constrained to one layer. We posit our investigations in the four-band continuum BLG–adatom Hamiltonian

$$\hat{H} = \begin{pmatrix} V + v_F \boldsymbol{\sigma} \cdot \hat{\mathbf{p}} & t_{\perp} \sigma_{-} \\ t_{\perp} \sigma_{+} & -V + v_F \boldsymbol{\sigma} \cdot \hat{\mathbf{p}} \end{pmatrix} + \sum_i \begin{pmatrix} v_0^i(\mathbf{r}) & 0 \\ 0 & 0 \end{pmatrix}, \quad (2)$$

where  $\hat{\mathbf{p}}$  is the two-dimensional (2D) kinematic momentum operator around Dirac point  $K$ ,  $v_F \approx 10^6$  m/s is the Fermi velocity,  $\sigma$  are Pauli matrices, with  $\sigma_z = \pm 1$  describing states residing on the  $A(B)$  sublattice, and  $\sigma_{\pm} = \sigma_x \pm i\sigma_y$ . The diagonal blocks in the first term on the right-hand side describe monolayers at a constant electrostatic energy,  $\pm V$  for top layer and bottom layer, respectively, whereas off-diagonal blocks contain the hopping processes  $A_2 \rightleftharpoons B_1$  connecting the two layers ( $t_{\perp} \approx 0.45$  eV) [48]. The bias potential  $V$  is determined from the experimental parameters according to  $V = -eDd/2\kappa$ , where  $-e < 0$  is the electron's charge,  $d \approx 0.35$  nm is the layer separation, and  $\kappa = 4$  is the phenomenological BLG effective permittivity [39, 49]. Diagonalization of the first term yields 2+2 bands separated by a gap:  $\Delta = 2|V|t_{\perp}/\sqrt{t_{\perp}^2 + 4V^2} \approx 2|V|$ . Their dispersion relation reads  $\epsilon^{\pm\pm}(\boldsymbol{\pi}) = \pm\sqrt{t_{\perp}^2/2 + \boldsymbol{\pi}^2 + V^2 \pm \lambda^2(\boldsymbol{\pi})}$ , where  $\boldsymbol{\pi} \equiv v_F \mathbf{p}$  and  $\lambda^2(\boldsymbol{\pi}) = \sqrt{t_{\perp}^4/4 + \boldsymbol{\pi}^2(t_{\perp}^2 + 4V^2)}$ . The second term is the scattering potential due to fluorine adatoms located in the top layer at random positions  $\{\mathbf{r}_i\}$  with  $v_0^i(\mathbf{r}) = v_0\delta(\mathbf{r} - \mathbf{r}_i)$ . In the scattering problem, outgoing and incoming wavefunctions are related by the  $T$  matrix [50]. For delta-peak potentials, outgoing waves from a single impurity at the origin acquire the simple form  $\psi_{\text{scatt}}(\mathbf{r}) = \hat{G}_0(\mathbf{r}, E)\hat{T}_{\text{ad}}(E)\phi_{\mathbf{k}}(\mathbf{r})$ , where  $\phi_{\mathbf{k}}(\mathbf{r})$  denotes free incoming wave solutions with momentum  $\mathbf{k}$ , i.e.,  $\hat{H}_0|\phi_{\mathbf{k}}\rangle = E|\phi_{\mathbf{k}}\rangle$ , and  $\hat{G}_0(\mathbf{r}, E)$  is the propagator of pristine biased BLG,  $\hat{G}_0(\mathbf{r}, E) = \langle \mathbf{r} | (E - \hat{H}_0 + i\eta)^{-1} | \bar{0} \rangle$ , with  $\eta$  a real infinitesimal. In the (resonant) scattering limit of interest  $v_0 \rightarrow \infty$ , we easily find

$$\hat{T}_{\text{ad}}(E) = - \sum_{\chi=A_2, B_2} [g_{\chi}(E)]^{-1} |\chi\rangle \langle \chi|, \quad (3)$$

where  $g_{\chi}(E) \equiv \langle \chi | \hat{G}(\bar{0}, E) | \chi \rangle$ . We evaluated  $g_{\chi}(E)$  in the entire parameter space (refer to Supplemental Material); in the intermediate regime  $\sqrt{t_{\perp}^2 + V^2} > |E| > |V|$  (typically  $\sim 0.05$ – $0.5$  eV),

$$g_{A_2}(E) = (V - E) [\bar{\Theta}_{\Lambda}(E) + (E + V)^2 \Theta_{\text{reg}}(E)], \quad (4)$$

$$g_{B_2}(E) = (t_{\perp}^2 + V^2 - E^2)(E + V)\Theta_{\text{reg}}(E) + (V - E)\bar{\Theta}_{\Lambda}(E), \quad (5)$$

where

$$\begin{Bmatrix} \Theta_{\text{reg}}(E) \\ \bar{\Theta}_{\Lambda}(E) \end{Bmatrix} = \frac{1}{4\pi v_F^2} \frac{1}{A_+ + A_-} \begin{Bmatrix} \ln\left(\frac{A_+}{A_-}\right) - i\pi \\ \Psi(\Lambda) + i\pi A_+ \end{Bmatrix}. \quad (6)$$

In the above,  $A_{\pm} = \sqrt{4E^2V^2 + t_{\perp}^2(E^2 - V^2)} \pm (E^2 + V^2)$ ,  $\Psi(x) = \sum_{p=\pm 1} A_p \ln(-p + x^2/|A_p|)$ , and  $\Lambda = \hbar v_F/R$  is the high-energy cutoff defining an effective potential range  $R$  [32]. Crucially, for non-zero bias field  $|V| > 0$ , the  $T$  matrix is sensitive to carrier polarity  $\pm|E|$  [see Eqs. (4)–(5)]. This feature results from the top-bottom layer asymmetry induced by the adatoms and, as argued below, is the origin of the strong EHA observed.

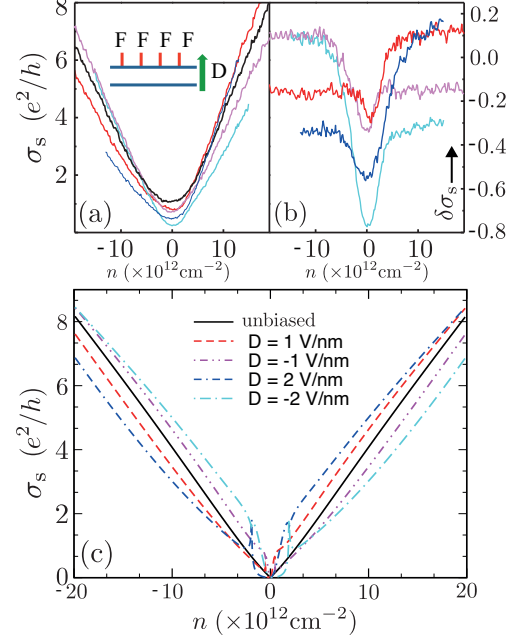


Figure 4: Tuning of charge carrier transport in  $D$ -field. (a) and (b)  $\sigma_s(n)$  and normalized conductance change  $\delta\sigma_s(D)$  for W02 at  $T = 1.6$  K and  $D = -2$  V/nm (cyan),  $-1$  V/nm (plum),  $0$  V/nm (black),  $1$  V/nm (red), and  $2$  V/nm (blue). Positive  $D$  points towards the fluorine adatoms as illustrated in the inset of (a). (c) Calculated dc-conductivity  $\sigma_s(n)$  for several inter-layer bias potentials corresponding to the  $D$ -field values in (a). Calculation only applies to  $n > n_F$ . Other parameters in main text.

The effect of dilute random adatoms in dc-transport is encoded in the inverse transport relaxation time

$$\frac{1}{\tau(\mathbf{k})} = \frac{2\pi n_F}{\hbar} \int \frac{d^2\mathbf{k}'}{(2\pi)^2} |\langle \phi_{\mathbf{k}} | \hat{T}_{\text{ad}}(E) | \phi_{\mathbf{k}'} \rangle|^2 \delta_{\mathbf{k}\mathbf{k}'}(E), \quad (7)$$

where  $\delta_{\mathbf{k}\mathbf{k}'}(E) \equiv (1 - \cos\theta_{\mathbf{k}\mathbf{k}'})\delta(\epsilon_{\mathbf{k}} - \epsilon_{\mathbf{k}'})$ ,  $\theta_{\mathbf{k}\mathbf{k}'}$  is the scattering angle, and  $\epsilon_{\mathbf{k}} \equiv \epsilon^{\pm-}(v_F\hbar\mathbf{k})$  for  $E = \pm|E|$ . The zero-temperature semiclassical dc-conductivity follows from  $\sigma_s = (e^2/h)k_F v(k_F)\tau(k_F)$ , where  $v(k) = |\nabla_{\mathbf{k}}\epsilon_{\mathbf{k}}|/\hbar$  is the band velocity and  $k_F$  is the Fermi wave vector [51]. In order to unbiasedly extract the model parameters  $n_F$  and  $R$ , we fit the 4-band expression to the  $D = 0$  conductivity data in the electron sector  $n > 0$  [see black curve in Fig. 4 (a)]. We obtain  $n_F \approx 1.6n_F^{\text{ram}}$  and  $R \approx 0.5$  nm, where  $n_F^{\text{ram}}$  is obtained from the Raman spectra of this device (see above). These parameters are then employed to evaluate  $\sigma_s(n)$  at all nonzero  $D$ -fields in Fig. 4 (c). The theory is seen to reproduce very well both the degree of EHA and the overall  $D$ -dependence observed in panel (a). This agreement is particularly remarkable as the strong scattering regime is characterized by a strong dependence of  $\tau^{-1}(\mathbf{k})$  in the  $D$ -field and model parameters. This robust agreement is strong evidence that the  $D$ -field tuning of the resonant

adatom scattering amplitudes (3) is responsible for the observed conductance modulation. Because of the resonant nature of the adatoms, a twofold change of the scattering cross section can lead to very large tuning of other resonant properties, such as the spin Hall angle [23], giving BLG-based systems a distinct advantage in graphene-based spintronics.

In summary, through a joint experiment–theory effort, we have demonstrated that a perpendicular electric field achieves substantial tuning of the amplitude of resonant impurity scattering in one-sided fluorinated bilayer graphene. Our findings set the stage for exploring all-electric control of resonant scatterings that underlie novel spintronics effects in graphenic materials.

*Acknowledgements.* We thank X. Hong for helpful discussions. A.S., J.L., and J.Z. are supported by ONR under Grant No. N00014-11-1-0730 and by NSF CAREER Grant No. DMR-0748604. A.F. and N.M.R.P. acknowledge EC under Graphene Flagship (Contract No. CNECT-ICT-604391). A.F. gratefully acknowledges the financial support of the Royal Society (U.K.) through a Royal Society University Research Fellowship. We acknowledge use of facilities at the PSU site of NSF NNIN.

---

\* Electronic address: [aires.ferreira@york.ac.uk](mailto:aires.ferreira@york.ac.uk)

† Electronic address: [jzhu@phys.psu.edu](mailto:jzhu@phys.psu.edu)

- [1] S. Stankovich, D. A. Dikin, G. H. B. Dommett, K. M. Kohlhaas, E. J. Zimney, E. A. Stach, R. D. Piner, S. T. Nguyen, and R. S. Ruoff, *Nature* **442**, 282 (2006).
- [2] Z. Luo, P. Vora, E. Mele, A. Johnson, and J. Kikkawa, *Appl. Phys. Lett.* **94**, 111909 (2009).
- [3] G. Eda, and M. Chhowalla, *Advanced Materials* **22**, 2392 (2010).
- [4] D. Elias, R. Nair, T. Mohiuddin, S. Morozov, P. Blake, M. Halsall, A. Ferrari, D. Boukhvalov, M. Katsnelson, and A. Geim, *Science* **323**, 610 (2009).
- [5] S. H. Cheng, K. Zou, F. Okino, H. Gutierrez, A. Gupta, N. Shen, P. Eklund, J. Sofo, and J. Zhu, *Phys. Rev. B* **81**, 205435 (2010).
- [6] B. Wang, J. R. Sparks, H. R. Gutierrez, F. Okino, Y. Tang, V. H. Crespi, J. O. Sofo and J. Zhu, *Appl. Phys. Lett.* **97**, 141915 (2010).
- [7] J. T. Robinson, J. S. Burgess, C. E. Junkermeier, S. C. Badescu, T. L. Reinecke, F. K. Perkins, M. K. Zalalutdinov, J. W. Baldwin, J. C. Culbertson, P. E. Sheehan, and E. S. Snow, *Nano Lett.* **10**, 3001 (2010).
- [8] R. R. Nair, W. C. Ren, R. Jalil, I. Riaz, V. G. Kravets, L. Britnell, P. Blake, F. Schedin, A. S. Mayorov, S. J. Yuan, M. I. Katsnelson, H. M. Cheng, W. Strupinski, L. G. Bulusheva, A. V. Okotrub, I. V. Grigorieva, A. N. Grigorenko, K. S. Novoselov, and A. K. Geim, *Small* **6**, 2877 (2010).
- [9] Z. H. Ni, L. A. Ponomarenko, R. R. Nair, R. Yang, S. Anissimova, I. V. Grigorieva, F. Schedin, P. Blake, Z. X. Shen, E. H. Hill, K. S. Novoselov, and A. K. Geim, *Nano Lett.* **10**, 3868 (2010).
- [10] O. Leenaerts, H. Peelaers, A. Hernandez-Nieves, B. Paratoens, and F. Peeters, *Phys. Rev. B* **82**, 195436 (2010).
- [11] J.-H. Chen, W. G. Cullen, C. Jang, M. S. Fuhrer, and E. D. Williams, *Phys. Rev. Lett.* **102**, 236805 (2009)
- [12] M. Klintonberg, S. Lebegue, M. I. Katsnelson, and O. Eriksson, *Phys. Rev. B* **81**, 085433 (2010).
- [13] H. Zhang, E. Bekyarova, J. W. Huang, Z. Zhao, W. Bao, F. Wang, R. C. Haddon, and C. N. Lau, *Nano Lett.* **11**, 4047 (2011).
- [14] F. Withers, T. H. Bointon, M. Dubois, S. Russo, and M. Craciun, *Nano Lett.* **11**, 3912 (2011).
- [15] B. Wang, J. Wang, and J. Zhu, *ACS Nano* **8**, 1862 (2014).
- [16] O. Yazyev, *Rep. Prog. Phys.* **73**, 056501 (2010).
- [17] X. Hong, S. H. Cheng, C. Herding, and J. Zhu, *Phys. Rev. B* **83**, 085410 (2011).
- [18] X. Hong, K. Zou, B. Wang, S. H. Cheng, and J. Zhu, *Phys. Rev. Lett.* **108**, 226602 (2012).
- [19] R. Nair, M. Sepioni, I.-L. Tsai, O. Lehtinen, J. Keinonen, A. Krasheninnikov, T. Thomson, and A. Grigorieva, *Nat. Phys.* **8**, 199 (2012).
- [20] J.-H. Chen, L. Li, W. G. Cullen, E. D. Williams, M. S. Fuhrer, *Nat. Phys.* **7**, 535 (2011).
- [21] K. M. McCreary, A. G. Swartz, W. Han, J. Fabian, and R. K. Kawakami, *Phys. Rev. Lett.* **109**, 186604 (2012).
- [22] J. Balakrishnan, G. Kok Wai Koon, M. Jaiswal, A. H. Castro Neto, and B. Ozyilmaz, *Nat. Phys.* **9**, 284 (2013).
- [23] A. Ferreira, T.G. Rappoport, M.A. Cazalilla, and A.H. Castro Neto, *Phys. Rev. Lett.* **112**, 066601 (2014).
- [24] J. Balakrishnan, G.K.W. Koon, A. Avsar, Y. Ho, J.H. Lee, M. Jaiswal, S.-J. Baeck, J.-H. Ahn, A. Ferreira, M.A. Cazalilla, A.H. Castro Neto, B. Ozyilmaz, *Nat. Comm.* **5**, 4748 (2014).
- [25] T. O. Wehling, M. I. Katsnelson, and A. I. Lichtenstein, *Chem. Phys. Lett.* **476**, 125 (2009).
- [26] V. M. Pereira, F. Guinea, J. M. B. Lopes dos Santos, N. M. R. Peres, and A. H. Castro Neto. *Phys. Rev. Lett.* **96**, 036801 (2006).
- [27] V. M. Pereira, J. M. B. Lopes dos Santos, and A. H. Castro Neto. *Phys. Rev. B* **77**, 115109 (2008).
- [28] E. V. Castro, M. P. L.-Sancho, and M. A. H. Vozmediano, *Phys. Rev. Lett.* **104**, 036802 (2010).
- [29] V. Haefner, J. Schindler, N. Weik, T. Mayer, S. Balakrishnan, R. Narayanan, S. Bera, and F. Evers, *Phys. Rev. Lett.* **113**, 186802 (2014).
- [30] P. M. Ostrovsky, I. V. Protopopov, E. J. König, I. V. Gornyi, A. D. Mirlin, and M. A. Skvortsov, *Phys. Rev. Lett.* **113**, 186803 (2014).
- [31] T. Stauber, N. M. R. Peres, and F. Guinea, *Phys. Rev. B* **76**, 205423 (2007).
- [32] A. Ferreira, J. Viana-Gomes, J. Nilsson, E. R. Mucciolo, N. M. R. Peres, and A. H. Castro Neto, *Phys. Rev. B* **83**, 165402 (2011).
- [33] A. Ferreira, and E. R. Mucciolo, *Phys. Rev. Lett.* **115**, 106601 (2015).
- [34] A. Fert, and P. M. Levy, *Phys. Rev. Lett.* **106**, 157208 (2011); Y. Niimi, M. Morota, D.H. Wei, C. Deranlot, M. Basletic, A. Hamzic, A. Fert, and Y. Otani. *ibidem* 126601 (2011).
- [35] D. Kochan, M. Gmitra, and J. Fabian, *Phys. Rev. Lett.* **112**, 116602 (2014).
- [36] R. E. Mapasha, A. M. Ukpung, and N. Chetty, *Phys. Rev. B* **85**, 205402 (2012).
- [37] D. Nafday, and T. Saha-Dasgupta, *Phys. Rev. B* **88**, 205422 (2013).
- [38] E. McCann, *Phys. Rev. B* **74**, 161403 (2006).

- [39] H. K. Min, B. Sahu, S. K. Banerjee, and A. H. MacDonald, Phys. Rev. B **75**, 155115 (2007).
- [40] Y. B. Zhang, T. T. Tang, C. Girit, Z. Hao, M. C. Martin, A. Zettl, M. F. Crommie, Y. R. Shen, and F. Wang, Nature **459**, 820 (2009).
- [41] K. Mak, C. Lui, J. Shan, and T. Heinz, Phys. Rev. Lett. **102**, 256405 (2009).
- [42] K. Zou, and J. Zhu, Phys. Rev. B **82**, 081407 (2010).
- [43] K. Zou, F. Zhang, C. Clapp, A. H. MacDonald, and J. Zhu, Nano Letters **13**, 369 (2013).
- [44] See Supplemental Material attached below for fabrication and characterizations of the fluorinated devices and details of the calculations.
- [45] M. M. Lucchese, F. Stavale, E. H. M. Ferreira, C. Vilani, M. V. O. Moutinho, R. B. Capaz, C. A. Achete, and A. Jorio, Carbon **48**, 1592 (2010).
- [46] A. Weisse, G. Wellein, A. Alvermann, and H. Fehske, Rev. Mod. Phys **78**, 275 (2006).
- [47] S. Yuan, H. De Raedt, and M. I. Katsnelson, Phys. Rev. B **82**, 235409 (2010).
- [48] E. V. Castro, K. S. Novoselov, S. V. Morozov, N. M. R. Peres, J. M. B. Lopes dos Santos, J. Nilsson, F. Guinea, A. K. Geim, and A. H. Castro Neto, J. Phys.: Condens. Matter **22** 175503 (2010).
- [49] A weak  $n$ -dependence of screening  $\kappa(n)$  arising from charge imbalance between the layers has been neglected.
- [50] B. A. Lippmann and J. Schwinger, Phys. Rev. **79**, 469 (1950).
- [51] Outside the intermediate density regime, the expression for the dc-conductivity must be generalized to account for band degeneracies; refer to Supplemental Material for full details.

## Supplemental Material for “Electrically tunable resonant scattering in fluorinated bilayer graphene”

We give details on the fluorination and characterization of the biased bilayer graphene devices, and provide comprehensive derivations of the main results discussed in the Rapid Communication. Additional material includes explicit formulae for scattering properties such as cross sections, and fully quantum-mechanical tight-binding calculations in very large disordered systems. In particular, we show that the dependence of the Kubo dc-conductivity with the bias field is in good qualitative agreement with the predictions from the four-band semiclassical calculation.

### Contents

<b>References</b>	<b>5</b>
<b>I. Fabrication and Characterization of Fluorinated Bilayer Graphene Devices</b>	<b>6</b>
A. Fluorination of Bilayer Graphene	6
B. Color Map of 4-Terminal Resistance	6
C. Electron–Hole Assymetry	7
<b>II. Solution of the Scattering Problem</b>	<b>7</b>

A. Propagator of Biased Bilayer Graphene	7
B. Lippmann-Schwinger Approach to the Scattering Problem	10
Solution in Region II	11
Solution in Regions I and III	12

### III. Boltzmann Transport Formulation in Biased Bilayer Graphene

13

### IV. Fully Quantum Mechanical Tight-Binding Calculations using the KPM

15

Density of States	15
DC-Conductivity	16

### V. Appendix A: Calculation of the Propagator in Coordinate Space

17

### VI. Appendix B: Calculation of the Pristine LDOS

17

### References

18

## I. FABRICATION AND CHARACTERIZATION OF FLUORINATED BILAYER GRAPHENE DEVICES

### A. Fluorination of Bilayer Graphene

All samples were fluorinated in a plasma asher (Metroline M4L) using  $\text{CF}_4$ . Defluorination was done by annealing the sample in  $\text{Ar}/\text{H}_2$  flow at  $360^\circ\text{C}$  for 12 hours. Compared to monolayer graphene, bilayer graphene is substantially harder to fluorinate, presumably due to a flatter topography. Three parameters, namely, the power  $p$ , the gas pressure  $P$  and the duration time  $T$ , control the fluorine coverage as well as the unintentional vacancy density. Empirical trials show that the ratio of fluorine density vs vacancy density is maximized to be roughly 4:1 under conditions of  $p=100\text{ W}$  and  $P=200\text{mTorr}$  (100 sccm of  $\text{CF}_4$  gas flow). At this setting, a  $T=5\text{ min}$  run produces approximately  $n_{\text{F}}=1 \times 10^{12}\text{cm}^{-2}$ .

### B. Color Map of 4-Terminal Resistance

We attribute the resistance peak [black line in Fig. 1(d), main text] to the charge neutrality point (CNP). Tracking its evolution with  $V_{\text{tg}}$ ,  $V_{\text{bg}}$  and the location of a minimum along the black line allows us to determine the gating efficiencies of the top and bottom gates  $\alpha_{\text{tg}}$  and  $\alpha_{\text{bg}}$ , respectively, and also the unintentional doping of the two gates,  $V_{\text{tg}}^0$  and  $V_{\text{bg}}^0$ , respectively. The total carrier density is  $n = \alpha_{\text{tg}}(V_{\text{tg}} - V_{\text{tg}}^0) + \alpha_{\text{bg}}(V_{\text{bg}} - V_{\text{bg}}^0)$ , and the electric displacement field is  $D = (D_{\text{tg}} + D_{\text{bg}})/2$ , where  $D_{\text{bg}} = (\alpha_{\text{bg}}e)/\epsilon_0(V_{\text{bg}} - V_{\text{bg}}^0)$

and  $D_{\text{tg}} = -(\alpha_{\text{tg}}e)/\epsilon_0(V_{\text{tg}} - V_{\text{tg}}^0)$ . Table I lists the pa-

rameters of all devices used in this study.

	W38	W02	W03	Df
$\alpha_{\text{tg}}(\times 10^{12} \text{ cm}^{-2}\text{V}^{-1})$	2.3	3.15	3.15	2.3
$\alpha_{\text{bg}}(\times 10^{12} \text{ cm}^{-2}\text{V}^{-1})$	2.44	3	3	0.065
$V_{\text{tg}0} \text{ (V)}$	-1.7	-3.7	-6	-1.3
$V_{\text{bg}0} \text{ (V)}$	-0.2	0.6	-3.1	-7.7
$I_D/I_G$	1.15	1.15	1.3	0.3
$I_D/I_G^{**}$	0.9	1.25	1.4	N.A.
$n_{\text{F}}(\times 10^{12} \text{ cm}^{-2})$	2.2	3.8	4.4	0.6

Table I: Device characteristics for 3 dilute fluorinated bilayer graphene samples (W38, W03, and W02) and one defluorinated bilayer graphene sample (Df). Parameters are described in the text. ID/IG\*\* indicates the expected ID/IG from resonant scattering fits.

### C. Electron–Hole Assymetry

The density difference between the dual-gated portion of a bilayer and the area underneath the metal electrodes, whose density is only controlled by the backgate, can lead to bipolar junctions that are more resistive than unipolar junctions. Similar phenomena were studied in monolayers [1]. In our dual-gated bilayer, increasing  $V_{\text{bg}}$  in the positive direction creates a n-doped region underneath the contact, which favors the conduction of electrons. This extrinsic electron–hole assymetry carries the same sign as the  $D$ -field controlled resonant impurity scattering discussed in the main text since a positive  $V_{\text{bg}}$  results in a positive  $D$ -field so care must be taken to differentiate between the two.

The junction induced electron–hole assymetry becomes less important as the contact become less intrusive. Compared to conventional bar-like devices (pristine Bi 9-2 and Bi 5 shown in Fig. 1), fluorinated bilayer W02 shown in the main text [Fig. 1(c)] is a van der Pauw geometry with minimally intrusive voltage probes on the current path. Naturally, we expect a small impact from the junction effect on W02. In Fig. 1, we plot  $R_{\text{odd}}$  vs electron density  $n$  of the dual-gated area at fixed  $n_{\text{bg}}$ , using

$$R_{\text{odd}}(n_{\text{bg}}) = \frac{1}{2} [R(n, n_{\text{bg}}) - R(-n, n_{\text{bg}})],$$

as a measure of the electron–hole assymetry [1]. Fig. 1(a)-(c) compare results from two pristine bilayer samples and the fluorinated W02 (in Fig. 4, main text). Bi 9-2 and Bi 5 use 300nm SiO<sub>2</sub> backgates so the carrier density and  $D$  field range are smaller than that of W02.

On the pristine devices,  $R_{\text{odd}}$  increases with the magnitude of  $n_{\text{bg}}$  and reverses sign in the vicinity of  $n_{\text{bg}} = 0$ , as expected from the junction effect. Furthermore,  $R_{\text{odd}}$  decreases with increasing  $n$  and tends toward zero at high

$n$ . In comparison,  $R_{\text{odd}}$  in W02, which is non-zero because it does exhibit electron–hole assymetry, does not correlate with  $n_{\text{bg}}$  and shows no dependence on  $n$ . This rules out the junction effect as the origin of the reported electron–hole assymetry tuning.

## II. SOLUTION OF THE SCATTERING PROBLEM

### A. Propagator of Biased Bilayer Graphene

In this section we provide the derivation of the propagator of low-energy quasi-particles in Bernal-stacked bilayer graphene in the presence of a perpendicular electric field. For our purposes it is sufficient to consider the following minimal Hamiltonian describing  $\pi$ -electrons in the  $K$  valley [3]

$$\hat{H}_K = \begin{matrix} B_2 \\ A_1 \\ B_1 \\ A_2 \end{matrix} \begin{pmatrix} V & 0 & 0 & \hat{\pi} \\ 0 & -V & \hat{\pi}^\dagger & 0 \\ 0 & \hat{\pi} & -V & -t_\perp \\ \hat{\pi}^\dagger & 0 & -t_\perp & V \end{pmatrix}, \quad (1)$$

where  $\hat{\pi} \equiv v_F(\hat{p}_x + i\hat{p}_y)$  [here  $\hat{\mathbf{p}} = -(i/\hbar)\nabla$  is the 2D momentum operator and  $v_F \approx 10^6 \text{ ms}^{-1}$  is the Fermi velocity],  $t_\perp$  denotes the inter-layer hopping, and  $V$  is half the energy difference between the layers as induced by a perpendicular electric field [4]. Hereafter we set  $\hbar \equiv 1$ . The dispersion relations of the four bands associated with  $\hat{H}_K$  read as

$$\epsilon^{\pm\pm}(\boldsymbol{\pi}) = \pm \sqrt{\frac{t_\perp^2}{2} + \boldsymbol{\pi}^2 + V^2} \pm \sqrt{\frac{t_\perp^4}{4} + \boldsymbol{\pi}^2 (t_\perp^2 + 4V^2)}, \quad (2)$$

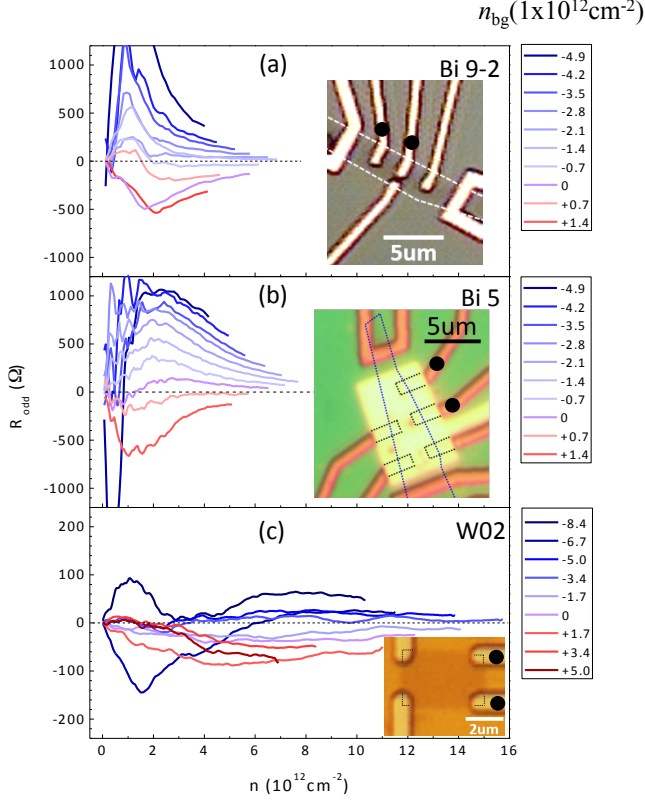


Figure 1: A close look into the electron–hole asymmetry.  $R_{\text{odd}}$  vs electron density  $n$  at selected  $n_{\text{bg}}$  for pristine bilayers Bi 9-2, Bi5 and fluorinated bilayer W02. (Bi9-2 and Bi 5 were reported in Ref. [2]). The magnification of the y-axis is adjusted to account for the geometry difference between the three measurements, ensuring a fair comparison. Positive  $n_{\text{bg}}$  corresponds to electrons. Insets are optical micrographs of the devices. The graphene flake is outlined in each image. Black dots indicate voltage probes used. In Bi9-2 and Bi 5, the voltage probes are fairly invasive with pronounced junction effect. They are minimally invasive in W02.

where  $\boldsymbol{\pi} = v_F \mathbf{p} \equiv v_F p (\cos \theta_{\mathbf{p}}, \sin \theta_{\mathbf{p}})^t$ . The presence of a bias potential opens a gap  $\Delta = 2|Vt_{\perp}|/\sqrt{4V^2 + t_{\perp}^2}$ .

Usually  $|V|$  is small, and thus  $\Delta \simeq 2|V|$  is a good approximation. Depending on the position of the Fermi level, three spectral regions must be considered:

- Region I:  $|V| > |E| > \Delta/2$ , the “Mexican hat” region. Here, the Fermi level crosses the band  $\epsilon^{\pm-}$  twice.
- Region II:  $E_H > |E| > \Delta/2$ , the intermediate density region where the Fermi level crosses  $\epsilon^{\pm-}$  at a single point.
- Region III:  $\Lambda > |E| > E_H$ , the high-energy region where the Fermi level crosses  $\epsilon^{\pm\pm}$  and  $\epsilon^{\pm-}$  at a single point.

In the above,  $\pm E_H = \pm\sqrt{t_{\perp}^2 + V^2}$  denotes the maximum (minimum) of the band  $\epsilon^{\pm\pm}$  and  $\Lambda$  a cutoff of the low-energy theory (see below). In what follows we compute the propagator in coordinate space in regions I–III.

The resolvent operator  $\hat{G}(z) \equiv (z - \hat{H}_K)^{-1}$  has a simple representation in momentum space:

$$\mathcal{G}(z, \boldsymbol{\pi}) = \left[ z - \frac{t_{\perp}}{2} (\sigma_z \otimes \sigma_x - \sigma_0 \otimes \sigma_x) - |\boldsymbol{\pi}| \sigma_x \otimes (\mathbf{n}' \cdot \boldsymbol{\sigma}) - V \sigma_z \otimes \sigma_z \right]^{-1}, \quad (3)$$

where  $\mathbf{n}' = (\cos \theta_{\mathbf{p}}, -\sin \theta_{\mathbf{p}})^t$ ,  $\sigma_{\alpha}$  are Pauli matrices ( $\alpha = x, y, z$ ), and  $\sigma_0$  is the  $2 \times 2$  identity. The matrix inversion in (3) is straightforward. We obtain

$$\mathcal{G}(z, \boldsymbol{\pi}) = \frac{1}{D(z, \boldsymbol{\pi})} \mathcal{D}^{(4)}(z, \boldsymbol{\pi}), \quad (4)$$

where

$$\begin{aligned} D(z, \boldsymbol{\pi}) &\equiv - \prod_{\lambda, \lambda' = \pm 1} [z - \epsilon^{\lambda \lambda'}(\boldsymbol{\pi})] \\ &= -\boldsymbol{\pi}^4 + 2\boldsymbol{\pi}^2(z^2 + V^2) \\ &\quad + (z^2 - V^2)(t_{\perp}^2 - z^2 + V^2), \end{aligned} \quad (5)$$

and  $\mathcal{D}^{(4)}(z, \boldsymbol{\pi})$  is the matrix

$$\mathcal{D}^{(4)}(z, \boldsymbol{\pi}) = \begin{pmatrix} \Xi_{1+}(z, \boldsymbol{\pi}) & \boldsymbol{\pi}^2 e^{2i\theta_{\mathbf{p}}} t_{\perp} & \boldsymbol{\pi} e^{i\theta_{\mathbf{p}}} t_{\perp} (z + V) & \boldsymbol{\pi} e^{i\theta_{\mathbf{p}}} \Upsilon_{+}(z, \boldsymbol{\pi}) \\ \boldsymbol{\pi}^2 e^{-2i\theta_{\mathbf{p}}} t_{\perp} & \Xi_{1-}(z, \boldsymbol{\pi}) & \boldsymbol{\pi} e^{-i\theta_{\mathbf{p}}} \Upsilon_{-}(z, \boldsymbol{\pi}) & \boldsymbol{\pi} e^{-i\theta_{\mathbf{p}}} t_{\perp} (z - V) \\ \boldsymbol{\pi} e^{-i\theta_{\mathbf{p}}} t_{\perp} (z + V) & \boldsymbol{\pi} e^{i\theta_{\mathbf{p}}} \Upsilon_{-}(\boldsymbol{\pi}) & \Xi_{2+}(z, \boldsymbol{\pi}) & t_{\perp} (z^2 - V^2) \\ \boldsymbol{\pi} e^{-i\theta_{\mathbf{p}}} \Upsilon_{+}(z, \boldsymbol{\pi}) & t_{\perp} (z - V) \boldsymbol{\pi} e^{i\theta_{\mathbf{p}}} & t_{\perp} (z^2 - V^2) & \Xi_{2-}(z, \boldsymbol{\pi}) \end{pmatrix}. \quad (6)$$



In the above we have also defined the following quantities

$$\Upsilon_{\pm}(\boldsymbol{\pi}) = \boldsymbol{\pi}^2 - (z \pm V)^2, \quad (7)$$

$$\Xi_{1\pm}(\boldsymbol{\pi}) = (t_{\perp}^2 + V^2 - z^2)(z \pm V) + \boldsymbol{\pi}^2(z \mp V), \quad (8)$$

$$\Xi_{2\pm}(\boldsymbol{\pi}) = (z \pm V)\Upsilon_{\mp}(z, \boldsymbol{\pi}). \quad (9)$$

The propagator in coordinate space is obtained from (4) via inverse Fourier transform

$$G(z, \mathbf{r} - \mathbf{r}') = \int \frac{d\mathbf{p}}{4\pi^2} e^{i\mathbf{p}\cdot(\mathbf{r}-\mathbf{r}')} \mathcal{G}(z, v_F \mathbf{p}). \quad (10)$$

In order to evaluate the above integral we use differentiation under the integral sign, that is,

$$G(z, \mathbf{r} - \mathbf{r}') = \mathcal{D}^{(4)} \left( z, \frac{\nabla}{i} \right) \Lambda_0^{(4)}(z, \mathbf{r} - \mathbf{r}'), \quad (11)$$

with

$$\begin{aligned} \Lambda_0^{(4)}(z, \mathbf{r} - \mathbf{r}') &= \int \frac{d\mathbf{p}}{4\pi^2} \frac{e^{i\mathbf{p}\cdot(\mathbf{r}-\mathbf{r}')}}{D(z, p)} \\ &= \int_0^{\infty} \frac{dp p}{2\pi} \frac{J_0(p|\mathbf{r} - \mathbf{r}'|)}{D(z, v_F p)}. \end{aligned} \quad (12)$$

We note that the operation (11) is strictly valid for  $|\mathbf{r} - \mathbf{r}'| \neq 0$ , where the inverse Fourier transform (10) converges for all matrix components of  $\mathcal{G}$ . The one-dimensional integral in Eq. (12) can be solved using standard methods (we provide a derivation in the Ap-

pendix A). One obtains

$$\begin{aligned} \Lambda_0^{(4)}(E, \mathbf{r}) &= \frac{1}{4v_F^2} \frac{1}{A_+ + A_-} \times \\ &\begin{cases} -iH_0(p_+r) + \frac{2}{\pi} K_0(p_-r) & , A_- > 0 \text{ (regions II)} \\ -iH_0(p_+r) + iH_0(p_-r) & , A_- < 0 \text{ (regions I and III)} \end{cases}, \end{aligned} \quad (13)$$

where  $p_{\pm} = \sqrt{|A_{\pm}|}/v_F$  and

$$A_{\pm} = \pm(E^2 + V^2) + \sqrt{4E^2V^2 + t_{\perp}^2(E^2 - V^2)}. \quad (14)$$

In the above,  $H_0(\cdot)$  [ $K_0(\cdot)$ ] denotes the zeroth order first kind Hankel [second kind modified Bessel] function. In region II,  $\Lambda_0^{(4)}(E, \mathbf{r})$  contains one propagating mode  $H_0(p_+r)$ —representing outgoing cylindrical waves with momentum  $p_+$ —and one evanescent wave  $K_0(p_-r)$ . Regions I and III admit two (real) propagating solutions as the Fermi level intersects the electronic bands at two distinct points [namely,  $E = \epsilon^{\pm-}(v_F p_+)$  and  $E = \epsilon^{\pm-}(v_F p_-)$  in region I and  $E = \epsilon^{\pm-}(v_F p_+)$  and  $E = \epsilon^{\pm+}(v_F p_-)$  in region III].

Next, we show how to compute the propagator at the origin,  $G(E, \mathbf{r} = 0)$ . This quantity plays a central role in scattering from short-range impurities (Sec. II B). Combining Eqs. (4)-(6) and (10) we obtain

$$G(E, 0) = \int_0^{\infty} \frac{dp}{2\pi} \frac{p}{D(E, p) + i\eta} \begin{bmatrix} \Xi_{1+}(v_F p) & 0 & 0 & 0 \\ 0 & \Xi_{1-}(v_F p) & 0 & 0 \\ 0 & 0 & \Xi_{2+}(v_F p) & t_{\perp}(E^2 - V^2) \\ 0 & 0 & t_{\perp}(E^2 - V^2) & \Xi_{2-}(v_F p) \end{bmatrix}. \quad (15)$$

Since the matrix entries on the RHS are of the form  $a + bp^2$  we are lead to the following type of integrals

$$\Theta(E) \equiv \int_0^{\infty} \frac{dp}{2\pi} \frac{p}{D(E, p) + i\eta}, \quad (16)$$

$$\Theta_{\Lambda}(E) \equiv \int_0^{\frac{\Lambda}{v_F}} \frac{dp}{2\pi} \frac{p^3}{D(E, p) + i\eta}, \quad (17)$$

with  $\eta$  a real infinitesimal. We notice that the terms  $bp^2$  result in logarithmically divergent integrals and hence a cut-off was introduced in  $\Theta_{\Lambda}(E)$ . It is useful to recast

the denominator in the following form

$$\begin{aligned} \frac{1}{D(E, p) + i\eta} &= \frac{1}{A_- + A_+} \times \\ &\left( \frac{1}{A_- + v_F^2 p^2 + i s_- 0^+} + \frac{1}{A_+ - v_F^2 p^2 + i 0^+} \right), \end{aligned} \quad (18)$$

where  $s_- \equiv \text{sign}(A_-)$ . Inserting (18) into (16)-(17), and making use of the Sokhotski-Plemelj formula, we arrive at

$$\begin{aligned} \Theta(E) &= \frac{1}{4\pi v_F^2} \frac{1}{A_+ + A_-} \times \\ &\begin{cases} \ln \left( \frac{A_+}{A_-} \right) - i\pi & , A_- \geq 0 \\ \ln \left( -\frac{A_+}{A_-} \right) & , A_- < 0 \end{cases}, \end{aligned} \quad (19)$$

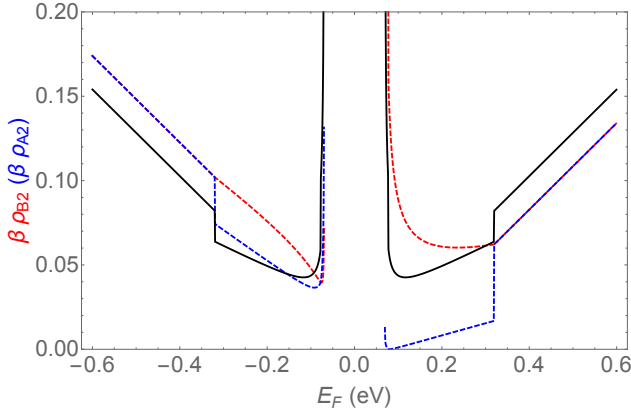


Figure 2: The local density of states per unit area at the bottom layer as function of energy (given in units of  $\beta^{-1} = t_{\perp}/v_F^2$ ). The LDOS on the top layer is obtained through reflexion, according to  $\rho_{B_1}(E) = \rho_{A_2}(-E)$  and  $\rho_{A_1}(E) = \rho_{B_2}(-E)$ . The total density of states is shown in solid line. Parameters as in Castro *et al.* Ref. [3]:  $V = 77.5$  meV,  $t_{\perp} = 0.1t$ , and  $t = 3.1$  eV.

$$\Theta_{\Lambda}(E) = -\frac{1}{4\pi v_F^4} \frac{1}{A_+ + A_-} \times \begin{cases} \Psi_+ \left( \frac{\Lambda}{v_F} \right) + i\pi A_+ & , A_- \geq 0 \\ \Psi_- \left( \frac{\Lambda}{v_F} \right) + i\pi(A_+ + A_-) & , A_- < 0 \end{cases}, \quad (20)$$

where

$$\Psi_{\pm}(x) = A_- \ln \left( \pm 1 + \frac{v_F^2 x^2}{|A_-|} \right) + A_+ \ln \left( -1 + \frac{v_F^2 x^2}{A_+} \right), \quad (21)$$

encodes the cutoff-sensitive component. The non-zero entries of Eq. (15) become

$$G(E, 0)_{1,1} = (t_{\perp}^2 + V^2 - E^2) + (E + V)\Theta(E) + v_F^2(E - V)\Theta_{\Lambda}(E), \quad (22)$$

$$G(E, 0)_{2,2} = (t_{\perp}^2 + V^2 - E^2)(E - V)\Theta(E) + v_F^2(E + V)\Theta_{\Lambda}(E), \quad (23)$$

$$G(E, 0)_{3,4} = t_{\perp}(E^2 - V^2)\Theta(E), \quad (24)$$

$$G(E, 0)_{4,3} = t_{\perp}(E^2 - V^2)\Theta(E), \quad (25)$$

$$G(E, 0)_{3,3} = (E + V)[v_F^2\Theta_{\Lambda}(E) - (E - V)^2\Theta(E)], \quad (26)$$

$$G(E, 0)_{4,4} = (E - V)[v_F^2\Theta_{\Lambda}(E) - (E + V)^2\Theta(E)]. \quad (27)$$

We remark that the local density of states (LDOS) can be obtained through a very similar calculation, according to  $\rho_{ii}(E) = (-1/\pi)\text{Im} G^+(E, 0)_{i,i}$  with  $G^+(E, 0) \equiv G(E + i0^+, 0)$ . The different form of the analytic continuation leads to somewhat different expressions (see Appendix B for details). The LDOS of a representative system is shown in Fig. 2.

## B. Lippmann-Schwinger Approach to the Scattering Problem

We are interested in scattering potentials of the form  $V_{\text{ad}}(\mathbf{r}) = \mathcal{V}\delta(\mathbf{r})$ , where  $\mathcal{V}$  is a Hermitian matrix encoding the action of the impurity in the bilayer. The scattering problem can be solved straightforwardly using the Lippmann-Schwinger (LS) equation [6], which for delta-peak potentials acquires the simple form

$$\Psi_{\mathbf{k}}(\mathbf{r}) = \phi_{\mathbf{k}}(\mathbf{r}) + G(E, \mathbf{r})\mathcal{V}\Psi_{\mathbf{k}}(0), \quad (28)$$

where  $\phi_{\mathbf{k}}(\mathbf{r})$  stands for the incident wave of energy  $E$  and momentum  $\mathbf{k}$ , whereas  $\Psi_{\mathbf{k}}(\mathbf{r})$  represents the full 'incident + scattered' wavefunction. Setting  $\mathbf{r} = 0$  in the LS equation results in

$$\Psi_{\mathbf{k}}(0) = [\mathbb{I} - G(E, 0)\mathcal{V}]^{-1} \phi_{\mathbf{k}}(0), \quad (29)$$

where  $G(E, 0)$  has been computed earlier (refer to Sec. II A). The scattered wavefunction  $\Delta\Psi_{\mathbf{k}}(\mathbf{r}) \equiv \Psi_{\mathbf{k}}(\mathbf{r}) - \phi_{\mathbf{k}}(\mathbf{r})$  is obtained by substituting (29) into the RHS of Eq. (28), i.e.,

$$\Delta\Psi_{\mathbf{k}}(\mathbf{r}) = G(E, \mathbf{r})\mathcal{V}[\mathbb{I} - G(E, 0)\mathcal{V}]^{-1} \phi_{\mathbf{k}}(0). \quad (30)$$

Local electrostatic potentials are described by a diagonal matrix in the sublattice space [5]

$$\mathcal{V} = V_0 \begin{bmatrix} a & 0 & 0 & 0 \\ 0 & b & 0 & 0 \\ 0 & 0 & c & 0 \\ 0 & 0 & 0 & d \end{bmatrix}, \quad (31)$$

where  $V_0 \equiv Sv_0$  with  $S$  encoding the areal range of the potential and  $v_0$  its strength. Denoting  $g_{n_1 n_2} \equiv [G(E, 0)]_{n_1, n_2}$  and inserting the potential matrix (31) into the LS equation (30) we obtain

$$\Delta\Psi_{\mathbf{k}}(\mathbf{r}) = G(E, \mathbf{r}) \begin{bmatrix} \frac{a}{V_0^{-1} - ag_{11}} & 0 & 0 & 0 \\ 0 & \frac{b}{V_0^{-1} - bg_{22}} & 0 & 0 \\ 0 & 0 & \frac{c(1 - dg_{44}V_0)}{\Phi(E)} & \frac{cdg_{34}V_0}{\Phi(E)} \\ 0 & 0 & \frac{cdg_{34}V_0}{\Phi(E)} & \frac{d(1 - cg_{33}V_0)}{\Phi(E)} \end{bmatrix} \phi_{\mathbf{k}}(0) \quad (32)$$

where

$$\Phi(E) = V_0^{-1} - dg_{44} - c[g_{33} + d(g_{34}^2 - g_{33}g_{44})V_0]. \quad (33)$$

Below we show how to compute the scattering flux for the particular case:  $b, c, d = 0 \wedge a = 1$ . The latter represents a potential localized on atom  $B_2$ , for which the intervalley terms have been artificially set to zero (see also remark [5]). Despite its simplicity, this model already contains the basic physics underpinning the electron-hole asymmetry observed in the experiments. For such a toy model,

the scattered component reads

$$\Delta\Psi_{\mathbf{k}}(\mathbf{r})|_{B_2} = G(E, \mathbf{r}) \begin{bmatrix} \frac{1}{V_0^{-1}-g_{11}} & 0 & 0 & 0 \\ 0 & 0 & 0 & 0 \\ 0 & 0 & 0 & 0 \\ 0 & 0 & 0 & 0 \end{bmatrix} \phi_{\mathbf{k}}(0). \quad (34)$$

### Solution in Region II

To make further progress we need the form of the incident wave. Taking the incoming momentum along the  $x$  axis, and assuming for simplicity  $|V| \leq |E| \leq E_H$  (region II), we have

$$\phi_{\mathbf{k}}(0)|_{\text{II}} = \mathcal{N}(E) \begin{bmatrix} \frac{v_F k}{E-V} \\ \frac{(E-V)(t_{\perp}^2 + V^2 - E^2) + v_F^2 k^2 (E+V)}{v_F k t_{\perp} (E-V)} \\ \frac{v_F^2 k^2 - (E-V)^2}{t_{\perp} (E-V)} \\ 1 \end{bmatrix}, \quad (35)$$

with  $\mathcal{N}(E)$  a normalization factor, whose form does not need to be specified. Altogether we have

$$\Delta\Psi_{\mathbf{k}}(\mathbf{r})|_{B_2} = \mathcal{N}(E)G(E, \mathbf{r}) \begin{bmatrix} \frac{v_F k}{E-V} \frac{1}{V_0^{-1}-g_{11}(E)} \\ 0 \\ 0 \\ 0 \end{bmatrix}. \quad (36)$$

All that is left is to ‘‘propagate’’ the wave by acting with  $G(E, \mathbf{r})$ . The propagator reads [refer to Eqs. (10)-(13)]

$$G(z, \mathbf{r}) = \mathcal{D}^{(4)} \left( z, \frac{\nabla}{i} \right) \Lambda_0^{(4)}(z, \mathbf{r}), \quad (37)$$

where  $\mathcal{D}^{(4)}$  is obtained from Eq. (6) replacing  $\boldsymbol{\pi} e^{\pm i\theta_{\mathbf{p}}} \rightarrow v_F(\hat{p}_x \pm i\hat{p}_y)$  and

$$\Lambda_0^{(4)}(z, \mathbf{r})|_{\text{II}} = \frac{1}{4v_F^2} \frac{1}{A_+ + A_-} \left[ -iH_0 \left( v_F^{-1} \sqrt{A_+} |\mathbf{r}| \right) + \frac{2}{\pi} K_0 \left( v_F^{-1} \sqrt{|A_-|} |\mathbf{r}| \right) \right]. \quad (38)$$

Inserting this expression into (37), and using  $H_0(x) \rightarrow \sqrt{\frac{2}{\pi x}} e^{i(x-\frac{\pi}{4})}$  for  $x \gg 1$ , we finally arrive at

$$\Delta\Psi_{\mathbf{k}}(r, \theta)|_{B_2} \xrightarrow{r \gg 1} -\frac{i}{8v_F^2} \frac{\mathcal{N}(E)}{\sqrt{4E^2V^2 + t_{\perp}^2(E^2 - V^2)}} \sqrt{\frac{2}{i\pi kr}} e^{ikr} \mathcal{D}^{(4)}(E, v_F k e^{i\theta}) \begin{bmatrix} \frac{v_F k}{E-V} \frac{1}{V_0^{-1}-g_{11}(E)} \\ 0 \\ 0 \\ 0 \end{bmatrix}, \quad (39)$$

where we have identified the wavevector at the point of observation [i.e.,  $\mathbf{k}' = k\mathbf{r}/r = k(\cos\theta, \sin\theta)^t$ ]. Equation (39) gives the exact asymptotic form of the scattered wavefunctions in the energy range  $|V| \leq |E| \leq E_H$ .

According to the definition of differential cross section [14] it follows that

$$\sigma(\theta) = r \left| \frac{v_n(r, \theta)}{v_{\text{in}}} \right|, \quad (40)$$

where  $v_{\text{in}} [v_n(r, \theta)]$  is the velocity of the incident wave [scattered wave], that is

$$v_{\text{in}} = v_F \langle \phi_{\mathbf{k}}(0) | \begin{pmatrix} 0 & 0 & 0 & 1 \\ 0 & 0 & 1 & 0 \\ 0 & 1 & 0 & 0 \\ 1 & 0 & 0 & 0 \end{pmatrix} | \phi_{\mathbf{k}}(0) \rangle, \quad (41)$$

$$v_n(r, \theta) = v_F \langle \Delta \Psi_{\mathbf{k}} | \begin{pmatrix} 0 & 0 & 0 & e^{i\theta} \\ 0 & 0 & e^{-i\theta} & 0 \\ 0 & e^{i\theta} & 0 & 0 \\ e^{-i\theta} & 0 & 0 & 0 \end{pmatrix} | \Delta \Psi_{\mathbf{k}} \rangle. \quad (42)$$

Substitution of (39) and (35) into the above expressions and subsequent use of (40) gives after somewhat lengthy but simple algebra:

$$\sigma(\theta) \Big|_{B_2}^{|V| \leq |E| \leq E_H} = \frac{1}{32\pi k} \frac{1}{4E^2V^2 + t_{\perp}^2(E^2 - V^2)} \frac{(\hbar^2 k^2 t_{\perp})^2}{\left| g_{11}(E) - \frac{\hbar^2}{SV_0} \right|^2} \frac{\Gamma(k, E, V)}{\Gamma(k, E, -V)}, \quad (43)$$

where

$$\Gamma(k, E, V) = t_{\perp}^2 v_F^2 k^2 (E + V) + \left[ v_F^2 k^2 - (E + V)^2 \right] \left[ (E - V)(v_F k)^2 + (E + V)(V^2 + t_{\perp}^2 - E^2) \right]. \quad (44)$$

The factor that controls the electron-hole asymmetry is easily identified:

$$\chi(E) = \frac{1}{\left| g_{11}(E) - \frac{\hbar^2}{SV_0} \right|^2} \frac{\Gamma(k, E, V)}{\Gamma(k, E, -V)}. \quad (45)$$

Remarkably, when the resonant scattering limit  $V_0 \rightarrow \infty$  is taken at nonzero bias  $V \neq 0$ , the  $E \rightarrow -E$  invariance is not recovered. This is to be contrasted to the case of (i) resonant impurities acting on both layers, and (ii) resonant impurities in monolayer graphene, for which cross

sections are electron-hole symmetric [6].

### Solution in Regions I and III

In regions I and III, Eq. (18) admits two propagating poles because  $A_- < 0$ . This occurs because the Fermi level crosses the electronic bands at two distinct Fermi points; see Eq. (2) and comments therein. As a consequence the scalar propagator [Eq. (12)] is given by a superposition of two cylindrical waves (see Appendix A)

$$\Lambda_0^{(4)}(z, \mathbf{r}) \Big|_{|E| > E_H} = \frac{1}{8v_F^2} \frac{1}{\sqrt{4E^2V^2 + t_{\perp}^2(E^2 - V^2)}} [-iH_0(k_+|\mathbf{r}|) + iH_0(k_-|\mathbf{r}|)], \quad (46)$$

where

$$k_{\pm} = \frac{1}{v_F} \sqrt{(E^2 + V^2) \pm \sqrt{4E^2V^2 + t_{\perp}^2(E^2 - V^2)}} \quad (47)$$

denote the Fermi momenta. The expression for the propagator evaluated at the origin also changes because  $A_- < 0$  [refer to Eqs. (19)-(20)]. The wavefunction of

incident particles therefore admits two (degenerate) solutions

$$\phi_{\mathbf{k}}^{\pm}(0)|_{\text{I,III}} = \mathcal{N}_{\pm}(E) \begin{bmatrix} \frac{v_F k_{\pm}}{E-V} \\ \frac{(E-V)(t_{\perp}^2 + V^2 - E^2) + v_F^2 k_{\pm}^2 (E+V)}{v_F k_{\pm} t_{\perp} (E-V)} \\ \frac{v_F^2 k_{\pm}^2 - (E-V)^2}{t_{\perp} (E-V)} \\ 1 \end{bmatrix}. \quad (48)$$

For instance, admitting an impurity located at site  $B_2$  and an incident wave with  $k = k_+$ , we have

$$\Delta\Psi_{\mathbf{k}}(r, \theta)|_{B_2} = \sum_{\lambda=\pm} \Delta\Psi_{\mathbf{k}}^{(\lambda)}(r, \theta)|_{B_2}, \quad (49)$$

with

$$\Delta\Psi_{\mathbf{k}}^{(\pm)}(r, \theta)|_{B_2} \rightarrow \mp \frac{i}{8v_F^2} \frac{\mathcal{N}_{\pm}(E)}{\sqrt{4E^2V^2 + t_{\perp}^2(E^2 - V^2)}} \sqrt{\frac{2}{i\pi k_{\pm} r}} e^{ik_{\pm}r} \mathcal{D}^{(4)}(E, v_F k_{\pm} e^{i\theta}) \begin{bmatrix} \frac{v_F k_{\pm}}{E-V} \frac{1}{V_0^{-1} - g_{11}(E)} \\ 0 \\ 0 \\ 0 \end{bmatrix}. \quad (50)$$

The total cross section accounts for both the processes  $k_+ \rightarrow k_+$  and  $k_+ \rightarrow k_-$  according to

$$\sigma(\theta)|_{k=k_+} \equiv \sigma_+(\theta) = \sigma_{++}(\theta) + \sigma_{+-}(\theta), \quad (51)$$

$$\sigma_{\pm\pm}(\theta) = r \frac{|v_n^{\pm\pm}(r, \theta)|}{|v_{\text{in}}(k_+)|}, \quad (52)$$

where

$$v_n^{\pm\pm}(r, \theta) = v_F \langle \Delta\Psi_{\mathbf{k}}^{(\pm)} | \begin{pmatrix} 0 & 0 & 0 & e^{i\theta} \\ 0 & 0 & e^{-i\theta} & 0 \\ 0 & e^{i\theta} & 0 & 0 \\ e^{-i\theta} & 0 & 0 & 0 \end{pmatrix} | \Delta\Psi_{\mathbf{k}}^{(\pm)} \rangle. \quad (53)$$

Similar expressions hold for incoming waves with incoming momentum  $k_-$ . The explicit form of  $\sigma_{\pm}(\theta)$  is

$$\sigma_{\pm}(\theta)|_{B_2}^{\text{I,III}} = \frac{1}{32\pi k_{\pm}} \frac{1}{4E^2V^2 + t_{\perp}^2(E^2 - V^2)} \frac{(\hbar^2 t_{\perp} k_{\pm}^2)^2}{|g_{11}(E) - \frac{\hbar^2}{SV_0}|^2} \frac{\Gamma(k_{\pm}, E, V) + \Gamma(k_{\mp}, E, V)}{\Gamma(k_{\pm}, E, -V)}. \quad (54)$$

### III. BOLTZMANN TRANSPORT FORMULATION IN BIASED BILAYER GRAPHENE

In this section we compute the Boltzmann de-conductivity limited by fluorine adatoms located in the top layer. As discussed in the main text, fluorine adatoms act as resonant impurities with a range  $R \sim 0.4$  nm. Such short-range impurities with  $R \gtrsim a_0$ —where  $a_0$  de-

notes the carbon-carbon distance—are well described by a potential matrix

$$\mathcal{V}^{(\text{top})} = V_0 \begin{bmatrix} 1 & 0 & 0 & 0 \\ 0 & 0 & 0 & 0 \\ 0 & 0 & 0 & 0 \\ 0 & 0 & 0 & 1 \end{bmatrix}, \quad (55)$$

with the resonant limit  $V_0 \rightarrow \infty$  taken when appropriate [6]. The solution of the respective scattering problem is

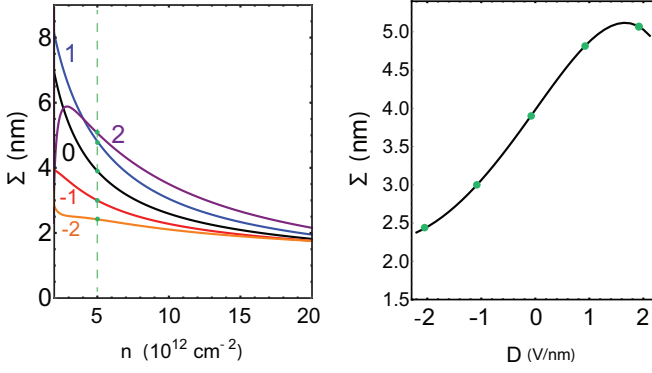


Figure 3: Electric field tuning of the transport cross section. Left panel—Cross section versus electronic density at selected values of the bias  $D$ -field ( $D = -2\kappa V/ed$ , indicated in V/nm). Right panel—Cross section versus bias field for  $n = 5 \times 10^{12} \text{ cm}^{-2}$ . (Other parameters as in the main text for sample W02.)

given by Eq. (32) with  $a = d = 1$  and  $b = c = 0$ . For example, in region II, one finds

$$\Delta\Psi_{\mathbf{k}}(r, \theta)|_{\text{top}} \xrightarrow{r \gg 1} \frac{i}{8v_F^2} \frac{\mathcal{N}(E)}{\sqrt{4E^2V^2 + t_{\perp}^2(E^2 - V^2)}} \sqrt{\frac{2}{i\pi kr}} e^{ikr} \mathcal{D}^{(4)}(E, v_F k e^{i\theta}) \begin{bmatrix} \frac{v_F k}{E-V} \frac{1}{g_{11}(E)} \\ 0 \\ 0 \\ \frac{1}{g_{44}(E)} \end{bmatrix}. \quad (56)$$

In the Boltzmann approach, the dc-conductivity is directly related to the cross sections of single scattering centres (computed in Sec. II) according to

$$\sigma_{\text{dc}}(k_F) = \frac{2e^2}{h} \times \begin{cases} \frac{k_F}{n_{\text{ad}}\Sigma(k_F)} & , \text{ region II} \\ \sum_{s=\pm} \frac{k_F^{(s)}}{n_{\text{ad}}\Sigma(k_F^{(s)})} & , \text{ otherwise} \end{cases}. \quad (57)$$

with  $n_{\text{ad}}$  denoting the areal density of adatoms. The transport cross section is given by

$$\Sigma(k_F^{(s)}) = \int_0^{2\pi} d\theta (1 - \cos\theta) |\sigma_s(\theta)|^2, \quad (58)$$

and a similar expression holds for region II, with  $\sigma(\theta)$  and  $\sigma_{\pm}(\theta)$  as defined earlier. The explicit expressions for  $\Sigma(k_F^{(s)})$  are rather cumbersome and will not be given here. We remark that the cross sections above are expected to match those of a hard wall disk of radius  $R \gtrsim a_0$ . The equivalence between the two scattering problems in monolayer and bilayer graphene has been demonstrated within a two-band description by some of the authors in Ref. [6]. To model the experiments it is useful to express the Fermi energy as a function of the electronic density

$$E(n) = \text{sign}(n) \times \begin{cases} \sqrt{\hbar^2 v_F^2 \pi |n| + \frac{t_{\perp}^2}{2} + V^2} - \sqrt{\frac{t_{\perp}^4}{4} + \hbar^2 v_F^2 \pi |n| (t_{\perp}^2 + 4V^2)} & , |V| \leq |E(n)| \leq E_H \\ \sqrt{\frac{\hbar^2 v_F^2 \pi |n|}{2} - V^2} & , |E(n)| > E_H \\ \sqrt{\frac{(\frac{\hbar^2 v_F^2 \pi n}{2})^2 + t_{\perp}^2 V^2}{t_{\perp}^2 + 4V^2}} & , \frac{\Delta}{2} < |E(n)| < |V| \end{cases}. \quad (59)$$

In deriving the above formulae we have used the relations

$$|n| = \frac{1}{\pi} \times \begin{cases} k_F^2 & , |V| \leq |E| \leq E_H \\ k_+^2 + k_-^2 & , |E| > E_H \\ k_+^2 - k_-^2 & , \frac{\Delta}{2} < |E| < |V| \end{cases}. \quad (60)$$

These expressions were used to make the plots of the dc-conductivity shown in the main text.

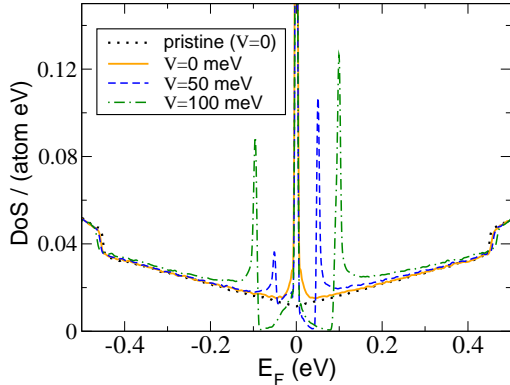


Figure 4: Average DOS of a real-size BLG system with  $D = 2 \times 14142^2$  carbon atoms at selected positive bias values for 0.05% vacancy concentration computed with Eq. (64).  $N = 20000$  Chebyshev moments have been used, resulting in superior meV resolution. The DOS of pristine unbiased system is shown as a guide to the eye. Other parameters:  $t = 2.7$  eV and  $t_{\perp} = 0.45$  eV.

In Fig. 3 we show the dependence of the cross section (58) on the electrostatic potential  $V$  and electronic density. A few important remarks are in order. For simplicity, we have only considered the resonant limit  $V_0 \rightarrow \infty$ . However, real fluorine induces a finite (strong) scalar potential  $V_0$ , which breaks the exact symmetry of our model  $\sigma_{dc}(n, V) = \sigma_{dc}(-n, -V)$ . The latter and the effect of bipolar junctions (see Sec. I) could explain why experiment [panel (a)] and theory [panel (c)] in Fig. 4 (main text) can only match perfectly for a given carrier polarity. Finally, we note that the full four-band model is required to correctly interpret the experiments, where  $v_{FP}$ ,  $V$  can be of the order of  $t_{\perp}$  and adatoms break the top bottom layer symmetry.

#### IV. FULLY QUANTUM MECHANICAL TIGHT-BINDING CALCULATIONS USING THE KPM

Fully quantum-mechanical calculations are performed using the kernel polynomial method (KPM) [7]. The use of KPM to compute electronic properties of graphene was introduced in Ref. [6] by some of the authors. Here, we briefly describe its application to biased bilayer graphene (BLG) systems.

The density of states is formally given by

$$\rho(E) = \frac{1}{D} \text{Tr} \delta(E - \hat{H}), \quad (61)$$

where  $\hat{H}$  is tight-binding Hamiltonian [8] and  $D$  is the dimension of the Hilbert space (i.e., number of lattice sites).

In the KPM approach, the—non-periodic—target function  $f(x)$  is expressed in terms of a complete set of orthogonal polynomials. First-kind Chebyshev polynomials  $\{T_n(x)\}_{n \in \mathbb{N}_0}$  are usually the best choice for systems with bounded spectrum [9, 46]. The use of Chebyshev polynomials requires rescaling the spectrum into the interval  $x \in [-1 : 1]$ , where a polynomial expansion  $f(x) = \sum_{\alpha} \alpha_n T_n(x)$  is defined with the following scalar product:

$$\alpha_n \equiv \langle T_n | f \rangle = \int_{-1}^1 \frac{dx}{\pi \sqrt{1-x^2}} T_n(x) f(x). \quad (62)$$

Application to the average DOS [Eq. (61)] is straightforward and results in

$$\rho(\epsilon) = \frac{2}{D\pi\sqrt{1-\epsilon^2}} \sum_{n=0}^{\infty} \frac{1}{1+\delta_{n,0}} \mu_n T_n(\epsilon), \quad (63)$$

where  $\epsilon \in [-1 : 1]$  is the rescaled energy, and the Chebyshev moments are given by  $\mu_n = \text{Tr} T_n(\tilde{H})$ , where  $\tilde{H} = \hat{H}/W$  and  $W$  is the half bandwidth of the biased bilayer system. In the KPM, the infinite sum in (63) is truncated and a kernel  $\{g_n\}_{n=0 \dots N-1}$  is introduced to damp Gibbs oscillations [7]

$$\rho_{\text{KPM}}(\epsilon) = \frac{2}{D\pi\sqrt{1-\epsilon^2}} \sum_{n=0}^{N-1} \frac{g_n}{1+\delta_{n,0}} \mu_n T_n(\epsilon), \quad (64)$$

where  $N$  depends on the desired resolution  $\eta$ , usually  $N \propto W/\eta$ . For the DOS we use the Jackson kernel due to its superior performance close to the Dirac point [6]

$$g_n = \frac{(N-n+1) \cos\left(\frac{\pi n}{N+1}\right) + \cot\left(\frac{\pi}{N+1}\right) \sin\left(\frac{\pi n}{N+1}\right)}{N+1}. \quad (65)$$

Finally, to compute the moments  $\mu_n$  efficiently we make use of the stochastic trace evaluation (STE) technique [10]. For large sparse matrices, the STE amounts to replace the trace  $\text{Tr}$  in Eq. (61) by the average with respect to a single random vector  $|R\rangle = \sum_{i=1 \dots D} \chi_i |i\rangle$ , that is,  $\text{Tr} T_n(\hat{H}) \rightarrow \langle R | T_n(\hat{H}) | R \rangle$ . The latter is essential exact for large sparse systems because fluctuations can be shown to be of the order of  $D^{-1/2}$ .

As explained in the main text, we model resonant adatoms by removing the corresponding  $p_z$  orbitals to

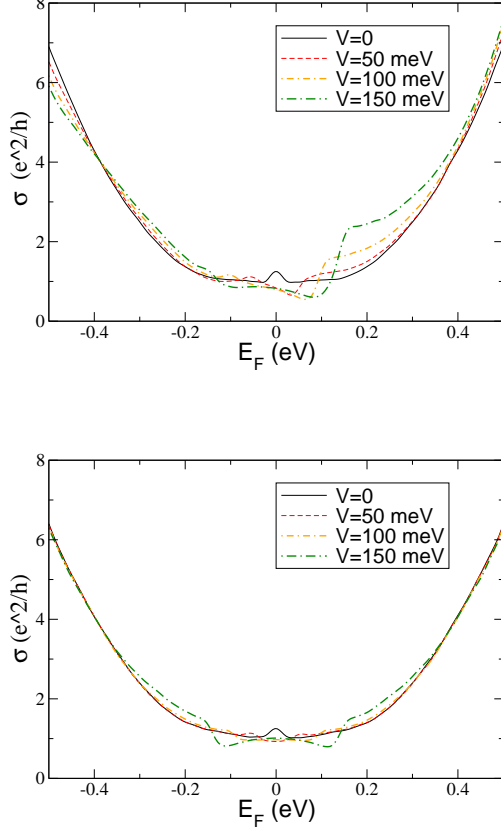


Figure 5: Kubo dc-conductivity of a BLG system with  $D = 2 \times 3200^2$  carbon atoms at selected bias values for 0.5% vacancy concentration [(top panel) vacancies distributed in the right layer; (bottom panel) vacancies distributed in the both layers]. The calculation has  $N^2 = 1000^2$  Chebyshev expansion coefficients and kernel resolution  $\eta = 15$  meV. Other parameters as in Fig. 4.

which they hybridize [6]. The average DOS of real-size bilayer graphene system with dilute vacancies in the top layer computed with this powerful technique is shown in Fig. 4 for several values of the bias inter-layer potential.

### DC-Conductivity

Next we discuss the application of KPM to the calculation of the dc-conductivity. The starting point is the Kubo formula at zero temperature [11]

$$\sigma_{\text{dc}}(E) = \frac{\pi g_s \hbar e^2}{\Omega} \text{Tr} \left[ \hat{v}_x \delta(E - \hat{H}) \hat{v}_x \delta(E - \hat{H}) \right], \quad (66)$$

where  $\hat{v}_x = (i/\hbar)[\hat{H}, \hat{x}]$  is the  $x$ -th component of the velocity operator,  $g_s = 2$  is a spin degeneracy factor, and  $\Omega$  stands for the area. In order to write  $\sigma_{\text{dc}}(E)$  in terms of Chebyshev polynomials, we rescale the energy variable

and operators in (66) to get

$$\sigma_{\text{dc}}(\epsilon) = \frac{\pi g_s \hbar e^2}{\Omega} \text{Tr} \left[ \tilde{v}_x \delta(\epsilon - \tilde{H}) \tilde{v}_x \delta(\epsilon - \tilde{H}) \right]. \quad (67)$$

The above formula has support in the interval  $[-1 : 1]$  and can now be written in terms of a KPM expansion as

$$\sigma_{\text{KPM}}(\epsilon) = \frac{2g_s \hbar e^2}{\pi \Omega (1 - \epsilon^2)} \sum_{n,m=0}^{N-1} \Delta_{nm} [T_{n+m}(\epsilon) + T_{|n-m|}(\epsilon)], \quad (68)$$

where the expansion coefficients

$$\Delta_{nm} \equiv \frac{g_n}{1 + \delta_{n,0}} \frac{g_m}{1 + \delta_{m,0}} \text{Tr} \left[ \tilde{v}_x T_n(\tilde{H}) \tilde{v}_x T_m(\tilde{H}) \right], \quad (69)$$

are computed with the STE technique, and a Lorentz kernel [7]

$$g_n = \frac{\sinh[\tilde{\eta}(N - n)]}{\sinh(\tilde{\eta}N)}, \quad (70)$$

is used to approximate the delta functions appearing in Eq. (67) by Lorentzians with resolution  $\eta \equiv \tilde{\eta}W$ . The computational cost of evaluating the matrix expansion coefficients in Eq. (69) is now substantially higher than computing DOS moments  $\mu_n = \text{Tr} T_n(\tilde{H})$ , which in practice limits the size of systems we can tackle.

In Fig. 5 we show the Kubo dc-conductivity for a BLG system with  $\sim 20$  million atoms [15]. The results disclose a conductivity plateau in the pseudo-gap region due to an impurity band formation, as found earlier in Ref. [6]. More importantly, the bias potential is seen to originate electron-hole asymmetry only for impurities restricted to a single layer, as discussed in the main text. Remarkably—away from the Dirac point—the conductivity displays the exact same trends as predicted by the semi-classical calculations. In particular, the linear response calculation shows that the increase of the conductivity upon increasing the bias field saturates in the electron sector ( $E_F > 0$ ), exactly as predicted by the 4-band semi-classical model (Sec. III). The opposite trends are observed upon reversal of the bias sign (not shown), again as predicted by the semi-classical calculation.



## V. APPENDIX A: CALCULATION OF THE PROPAGATOR IN COORDINATE SPACE

For completeness we show how to compute the integral

$$\Lambda_0^{(4)}(\mathbf{u}) = \int_0^\infty \frac{dp p}{2\pi} \frac{J_0(pu)}{D(z, v_F p) + i\eta}, \quad u \equiv |\mathbf{u}| > 0. \quad (71)$$

The sign of the infinitesimal  $\eta$  is chosen as to guarantee that  $\Lambda_0^{(4)}(\mathbf{u})$  represents an outgoing wave. Using Eq. (18) we split the integral into two contributions  $\Lambda_0^{(4)}(\mathbf{u}) = \Lambda_0^+(\mathbf{u}) + \Lambda_0^-(\mathbf{u})$ , where

$$\Lambda_0^\pm(\mathbf{u}) = \int_0^\infty \frac{dp p}{2\pi a} \frac{J_0(pu)}{A_\pm \mp v_F^2 p^2 + i0^+}, \quad (72)$$

and  $a = A_- + A_+$  is a constant. The cases  $A_- \geq 0$  have to be considered separately. When  $A_- > 0$  (region II), the term  $\Lambda_0^-(\mathbf{u})$  reads

$$\Lambda_0^-(\mathbf{u}) = \int_0^\infty \frac{dp p}{2\pi a} \frac{J_0(pu)}{A_- + v_F^2 p^2 + i0^+} = \frac{1}{a} K_0(\sqrt{A_-} u). \quad (73)$$

In the above we have made use of

$$\int_0^\infty dp p \frac{J_0(pu)}{p^2 + z^2} = K_0(zu) \quad , \quad \text{for } \text{Re } z > 0,$$

(see, e.g., Eq. EH II 96(58), Ref. [12]), whereas for  $A_- < 0$  (regions I and III) one finds [13]

$$\Lambda_0^-(u) = \int_0^\infty \frac{dp p}{2\pi a} \frac{J_0(pu)}{-|A_-| + v_F^2 p^2 - i0^+} = \frac{i\pi}{2a} H_0(\sqrt{|A_-|} u). \quad (74)$$

The term  $\Lambda_0^+(\mathbf{u})$  has the same form in all regions since  $A_+ > 0$ . We find

$$\Lambda_0^+(u) = \int_0^\infty \frac{dp p}{2\pi a} \frac{J_0(pu)}{A_+ - v_F^2 p^2 + i0^+} = -\frac{i\pi}{2a} H_0(\sqrt{A_+} u). \quad (75)$$

The meaning of all these terms is clear. Eqs. (74)-(75) represent propagating waves with the characteristic two-dimensional asymptotic behavior  $\propto e^{iku}/\sqrt{k}u$ , whereas (73) encodes an evanescent mode.

## VI. APPENDIX B: CALCULATION OF THE PRISTINE LDOS

The local density of states (LDOS) is formally given by

$$\rho(E) = -\frac{1}{\pi} \text{Im} \text{diag} \{G(z, 0)_{1,1}, \dots, G(z, 0)_{4,4}\} \Big|_{z \rightarrow E + i0^+}. \quad (76)$$

From Eq. (4) we obtain the LDOS as an integral over the momentum variable

$$\rho(E) = -\frac{1}{\pi} \text{Im} \int_0^\infty \frac{dp}{2\pi} \frac{p}{\prod_{\lambda, \lambda' = \pm 1} [E - \epsilon^{\lambda \lambda'} (v_F p) + i0^+]} \times \text{diag} \{ \Xi_{1+}(v_F p), \Xi_{1-}(v_F p), \Xi_{2+}(v_F p), \Xi_{2-}(v_F p) \}. \quad (77)$$

Using the Sokhotski–Plemelj formula and evaluating the imaginary part we get after straightforward integrations

$$\rho(E)_{1,1} = (t_\perp^2 + V^2 - E^2)(E + V)\Phi^+ + (E - V)\Phi_\Lambda^+ \quad (78)$$

$$\rho(E)_{2,2} = (t_\perp^2 + V^2 - E^2)(E - V)\Phi^+ + (E + V)\Phi_\Lambda^+ \quad (79)$$

$$\rho(E)_{3,3} = (E + V) [\Phi_\Lambda^+ - (E - V)^2 \Phi^+], \quad (80)$$

$$\rho(E)_{4,4} = (E - V) [\Phi_\Lambda^+ - (E + V)^2 \Phi^+], \quad (81)$$

with

$$\begin{bmatrix} \Phi^+ \\ \Phi_\Lambda^+ \end{bmatrix} = \frac{s_E}{4\pi v_F^2} \frac{1}{A_+ + A_-} \times \begin{cases} \begin{bmatrix} 1 \\ A_+ \end{bmatrix} & , \quad |V| \leq |E| \leq E_H \\ \begin{bmatrix} 2 \\ A_+ - A_- \end{bmatrix} & , \quad \frac{\Delta}{2} < |E| < |V| \\ \begin{bmatrix} 0 \\ A_+ + A_- \end{bmatrix} & , \quad |E| > E_H \end{cases} \quad (82)$$

Explicitly,

$$\begin{bmatrix} \Phi^+ \\ \Phi_\Lambda^+ \end{bmatrix} = \frac{s_E}{8\pi v_F^2} \frac{1}{\sqrt{4E^2V^2 + t_\perp^2(E^2 - V^2)}} \times \begin{cases} \begin{bmatrix} 1 \\ E^2 + V^2 + \sqrt{4E^2V^2 + t_\perp^2(E^2 - V^2)} \end{bmatrix}, & |V| \leq |E| \leq E_H \\ \begin{bmatrix} 2 \\ 2(E^2 + V^2) \end{bmatrix}, & \frac{\Delta}{2} < |E| < |V| \\ \begin{bmatrix} 0 \\ 2\sqrt{4E^2V^2 + t_\perp^2(E^2 - V^2)} \end{bmatrix}, & |E| > E_H \end{cases} .$$

\* Electronic address: [aires.ferreira@york.ac.uk](mailto:aires.ferreira@york.ac.uk)

† Electronic address: [jzhu@phys.psu.edu](mailto:jzhu@phys.psu.edu)

- [1] B. Huard, N. Stander, J. A. Sulpizio, and D. Goldhaber-Gordon, PRB **78**, 121402 (2008).
- [2] K. Zou and J. Zhu, PRB **82**, 081407R (2010).
- [3] E.V. Castro *et al.*, J. Phys. Condens. Matter **22**, 175503 (2010); J. Jung, and A. H. MacDonald, Phys. Rev. B **89**, 035405 (2014).
- [4] The minimal Hamiltonian neglects corrections arising from intra- and inter-layer second-next-neighbor hoppings, responsible for trigonal warping and electron-hole asymmetry of the band structure [3]. These terms play a minor role in electronic transport at the energies considered.
- [5] Local potentials with range  $R \lesssim a$ —where  $a$  denotes the lattice spacing—induce intervalley scattering and thus a rigorous scattering treatment requires dealing with the valley subspace explicitly. We note, however, that our interest is on adatoms having  $R \gtrsim a$ . For such potentials the current formalism is adequate provided the correct ansatz for  $\mathcal{V}$  is taken (see Sec. III and Ref. [6]). Furthermore, the Kubo conductivity within a tight-binding formulation (Sec. IV) is seen display the same trends observed in the semiclassical calculation, hence providing further support to our minimal low-energy model.
- [6] A. Ferreira, *et al.*, Phys. Rev. B **83** 165402 (2011).
- [7] A. Weisse, G. Wellein, A. Alvermann, and H. Fehske, Rev. Mod. Phys **78**, 275 (2006).
- [8] We use the following tight-binding model

$$\begin{aligned} \hat{H}_{\text{BLG}} = & \sum_{\langle i,j \rangle} \left( -ta_{i,1}^\dagger b_{j,1} - ta_{i,2}^\dagger b_{j,2} - t_\perp a_{i,1}^\dagger b_{j,2} + \text{H.c.} \right) \\ & + V \sum_i \sum_{L=1,2} (-1)^L \left( a_{i,L}^\dagger a_{i,L} + b_{i,L}^\dagger b_{i,L} \right), \end{aligned}$$

where  $a(b)_{i,L}^\dagger$  creates quasiparticles in site  $i$  in sublattice  $A(B)$  at bottom/top layer  $L = 1, 2$ ,  $t(t_\perp)$  is the  $A$ - $B$  intra(inter)-layer hopping integral, and  $2V$  is the potential difference across the layers. To distinguish electron-hole effects, intra- and inter-layer second-next-neighbor hoppings have been neglected [4].

- [9] Chebyshev and Fourier Spectral Methods, Second Revised Edition, J. P. Boyd (Dover Publications, 2001).
- [10] T. Iitaka, and T. Ebisuzaki, Phys. Rev. E **69**, 057701 (2004).
- [11] G. D. Mahan, Many-particle Physics, 3rd ed. (Springer, New York, 2000).
- [12] I.S. Gradshteyn and I.M. Ryzhik. *Table of Integrals, Series, and Products*, 7th Edition (Elsevier, Academic Press, 2007)
- [13] To obtain this result we make use of the analytic continuation

$$\int_0^\infty dp p \frac{J_0(p|\mathbf{r}|)}{z^2 + p^2} \Big|_{z=-ip_F+0^+} = K_0(-ip_F|\mathbf{r}| + 0^+), \quad (83)$$

where  $p_F = \sqrt{|A_-|}$ . To express the result in terms of Hankel functions we use the connecting formula  $K_0(w) = \frac{i\pi}{2} H_0(iw)$  [valid for  $-\pi < \text{Arg}(w) \leq \pi/2$  (see e.g., <http://dlmf.nist.gov/10.27>)] to obtain the desired result

$$\Lambda_0(\mathbf{r}) = \frac{i\pi}{2} H_0(p_F|\mathbf{r}|). \quad (84)$$

- [14] L. L. Schiff, Quantum Mechanics, 3rd ed. (McGraw-Hill, New York, 1968).
- [15] In order to reach the diffusive regime we have artificially increased the concentration of impurities as compared to the experimental determined values.